Air Force Institute of Technology

AFIT Scholar

12-2004

Design and Model Verification of an Infrared Chromotomographic Imaging System

Daniel A. LeMaster

Follow this and additional works at: https://scholar.afit.edu/etd

Part of the Atomic, Molecular and Optical Physics Commons

DESIGN AND MODEL VERIFICATION OF AN INFRARED

CHROMOTOMOGRAPHIC IMAGING SYSTEM

THESIS

Daniel A. LeMaster, Civilian

AFIT/GAP/ENP/04-06

DEPARTMENT OF THE AIR FORCE
AIR UNIVERSITY

AIR FORCE INSTITUTE OF TECHNOLOGY

Wright-Patterson Air Force Base, Ohio

APPROVED FOR PUBLIC RELEASE; DISTRIBUTION UNLIMITED

The views expressed in this thesis are those of the author and do not reflect the official policy or position of the United States Air Force, Department of Defense, or the United States Government.

AFIT/GAP/ENP/04-06

DESIGN AND MODEL VERIFICATION OF AN INFRARED

CHROMOTOMOGRAPHIC IMAGING SYSTEM

THESIS

Presented to the Faculty

Department of Engineering Physics

Graduate School of Engineering and Management

Air Force Institute of Technology

Air University

Air Education and Training Command

In Partial Fulfillment of the Requirements for the

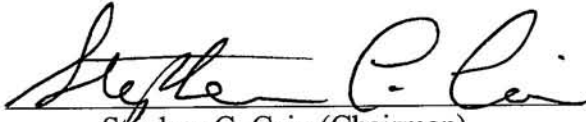Degree of Master of Science (Applied Physics)

Daniel A. LeMaster, BSE

December 2004

DESIGN AND MODEL VERIFICATION OF AN INFRARED

CHROMOTOMOGRAPHIC IMAGING SYSTEM

Daniel A. LeMaster, BSE
Civilian
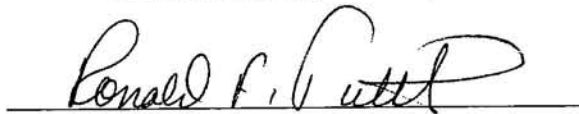
Approved:

_____   _____
Stephen C. Cain (Chairman)   16 Nov 04
                                              date

_____   _____
Glen P. Perram (Member)   16 NOV 04
                                              date

_____   _____
Ronald F. Tuttle (Member)   23 Nov 04
                                              date

AFIT/GAP/ENP/04-06

Abstract

A prism chromotomographic hyperspectral imaging sensor is being developed to aid in the study of bomb phenomenology. Reliable chromotomographic reconstruction depends on accurate knowledge of the sensor specific point spread function over all wavelengths of interest. The purpose of this research is to generate the required point spread functions using wave optics techniques and a phase screen model of system aberrations.

The phase screens are generated using the Richardson-Lucy algorithm for extracting point spread functions and Gerchberg-Saxton algorithm for phase retrieval. These phase screens are verified by comparing the modeled results of a blackbody source with measurements made using a chromotomographic sensor. The sensor itself is constructed as part of this research. Comparison between the measured and simulated results is based upon the noise statistics of the measured image.

Four comparisons between measured and modeled data, each made at a different prism rotation angle, provide the basis for the conclusions of this research. Based on these results, the phase screen technique appears to be valid so long as constraints are placed on the field of view and spectral region over which the screens are applied.

To My Father

Table of Contents

List of Figures

ix

List of Tables

DESIGN AND MODEL VERIFICATION OF AN INFRARED CHROMOTOMOGRAPHIC IMAGING SYSTEM

I. Introduction

Motivation

Bomb classification using remote sensing techniques presents a significant research challenge. Recent research at AFIT has linked the evolution of detonation spectra in time to the initial state of the ordinance with some success. (Orson and others, 2003:107)   In the future, these classification efforts using non-imaging techniques may be supplemented by analysis using hyperspectral techniques, specifically chromotomographic (CT) imaging technology.

The effectiveness of the CT imaging system, in terms of the spectral and spatial quality of the data product, is ultimately tied to the effectiveness of the data deconvolution algorithm. The original algorithm presented in the literature is incapable of reconstructing spectral information from images dominated by low spatial frequency structure (Mooney, 1997:2954).   To improve on this method, a new deconvolution algorithm is being developed which requires an explicit understanding of the point spread function (PSF) specific to the sensor.

1

Purpose

The purpose of this research is to assemble a CT imager, extract the phase information required to build appropriate point spread functions, and demonstrate the validity of these phase models through simulation and comparison with measured CT imagery.

Scope

The mid-wave infrared CT sensor is assembled and configured for use primarily in the laboratory to provide a validation of the wave optics simulation rather than a fully deployable sensor. Similarly, the phase retrieval algorithm used to generalize the PSF is intended to demonstrate the concept rather than provide a referendum on phase retrieval algorithms. The simulation approximates the propagation of light in terms of Fourier transforms.

Organization

Progression of this document follows, for all intents and purposes, the chronological development of the research. Chapter II contains background information on hyperspectral imaging systems and specific background on the CT system. The CT background is broken down into principles of chromotomographic imaging and a historical prospective of CT development.

Chapter III explains the sensor design and construction process. Prism selection and general optical system criteria are explained in terms of geometric optics. This chapter also contains an explanation of the component selection process and a detailed description of sensor assembly.

Chapter IV contains the theory behind the propagation model. The chapter begins with an explanation of Fourier propagation and image formation in terms of the point spread function. Later, the role of the aberration phase screen is described. The chapter concludes with an explanation of the prism transformation model and composite image formation. Other topics of interest include spatial and spectral sampling.

Chapter V deals with the two algorithms required to generate phase screens from measurements of intensity. This discussion includes the laboratory setup required to extract a point spread function using the Richardson-Lucy algorithm as well as a description of the algorithm itself. The second algorithm, the Gerchberg-Saxton phase retrieval algorithm, is discussed in terms of its functional form and how it generalizes the point spread function extracted using the Richardson-Lucy algorithm.

Chapter VI describes the noise statistics of the camera, the data measurement process, and the parameters used to fit the data. The statistical argument is based upon the assertions of other researchers as well as experimental data specific to the camera. The measurement process is presented together with the fit parameters because the methodology behind one helps to explain the other.

Chapter VII contains the experimental results with analysis and the conclusions reached during this research. Four comparisons of measured and simulated broadband CT images are used in this analysis. The results of each comparison are expressed in terms of the statistics of the measured image. Further discussion is devoted to the parameters used in the CT model to approximate the measured data in each of the four cases.

II. Background

Hyperspectral Imaging Systems

Traditional non-imaging spectrometers provide a spectrum formed as a conglomeration of emission from all points in the sensor's field of view. A Fourier transform interferometer, such as the one used in the bomb phenomenology research referenced previously, is an example of this type of sensor. By contrast, hyperspectral imaging (HSI) systems perform the same function over the field of view of each individual pixel in the sensor's focal plane array. The result is that each pixel in an HSI formed image contains its own independent spectrum. Hyperspectral and multispectral sensors come in two common varieties, those in the filter and scanning slit category, and a third emerging variety, the chromotomographic imager.

The product provided by the HSI sensor at any instant in time is commonly referred to as the data cube. Two dimensions of this cube form a plane that corresponds to the spatial dimensions of the sensor's overall field of view and, consequently, each pixel in this plane has a field of view equal to the total sensor field of view divided by the total number of pixels (assuming 100% fill factor). The value assigned to each pixel in this plane represents the flux incident on the sensor over a small portion of the spectrum. The cube's third dimension identifies spectral position and has a length equal to the spectral bandwidth of the sensor divided by the spectral resolution of the sensor. Figure 1 is a graphical representation of the data cube concept.

4
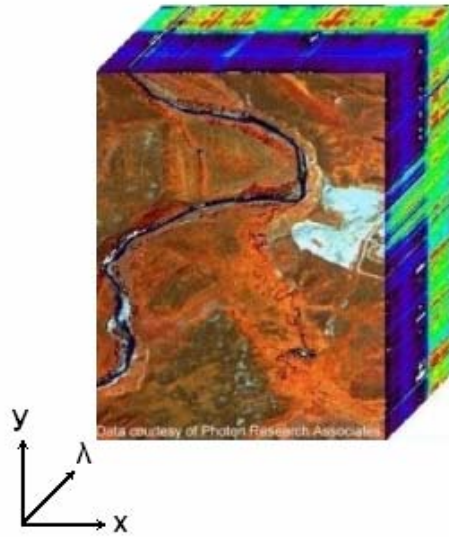
Figure 1: The Hyperspectral Data Cube (Modified from ITRES,2004)

The cube concept is useful for describing how hyperspectral data can be exploited. When the cube is integrated along the λ axis, the resulting image is akin to a traditional black and white photograph. Alternatively, the response of one pixel can be plotted against λ and the result is a spectrum similar to what would be obtained by a non-imaging spectrometer. Furthermore, individual horizontal slices or integrated slices can be searched separately for identifying features that are not readily apparent in traditional imagery. The potential value of these types of analysis is compounded when the scene in question is allowed to evolve in time though the collection of a series of data cubes.

Principles of the Direct Vision Prism CT

A polychromatic, collimated signal enters the prism assembly and is dispersed about a central, undeviated wavelength. The dispersed signal is collected via a focusing lens and projected upon a focal plane array. This process is updated continuously as the prisms rotate but the sensor is otherwise held fixed on the scene. As the prisms turns,

5

individual frames of the dispersed image are collected and stored for analysis. Essentially, each recorded frame contains a superposition of many monochromatic slices of the image offset from their original position based upon the dispersive properties and angle of rotation of the direct vision prism. Figure 2 is a graphical representation of this process.
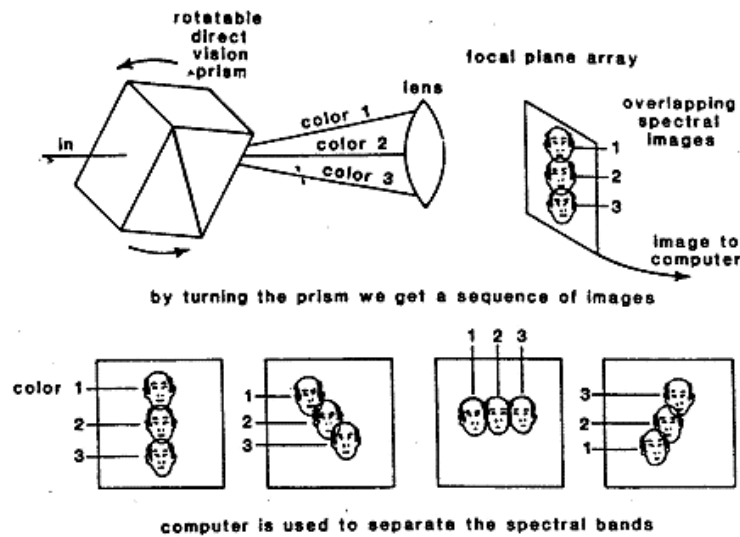
Figure 2. CT Image Formation Process (Mooney, 1995:66)

Once the image sequence is collected, the convoluted image can be rebuilt using an image reconstruction algorithm. Though reconstruction algorithms vary in the details, most rely on the notion that the dispersed image can be expressed mathematically as a "linear superposition of each spectral image convolved with a unique point spread function." (Mooney, 1995: 67) Equipped then with the dispersion and rotation angles of the prisms and specific knowledge of the point spread function, the hyperspectral data

6

cube can be reconstructed despite the unavoidable presence of noise, which is a significant complicating factor.

Historical Perspective on the CT

Though a variety of CT imaging systems were developed somewhat earlier, the direct vision prism MWIR chromotomographic camera, which is the basis for this research, was first developed by Jonathan Mooney at Rome Laboratory, Hanscom Air Force Base, in the mid 1990's. (Mooney and others, 1997:2951) Mooney states that his development trades computational overhead (the image reconstruction algorithm requires significant resources) for relatively high photon throughput and temporal resolution when compared to modern filter or slit based hyperspectral imaging systems. Mooney's reported design separated the 3-5 um portion of the MWIR band into 25 sub-bands over a 100 x 100 pixel focal plane array.

More recently, James Murguia of Solid State Scientific Corporation (in conjunction with Mooney and others) published a description of a visible/near IR CT imager capable of producing 64 spectral bands with a frame rate of 10 Hz. (Murguia, 2000:457) Currently, Sold State Scientific commercially offers visible, MWIR, and LWIR versions of the CT via their website. (CTHIS, 2004)

Two AFIT theses on CT imaging precede this work. The first was an attempt to simulate basic point spread functions generated by a notional chromotomographic imager to aid in sensor design and image reconstruction (these are goals not unlike those presented here, but on a much more modest scale). (Dearinger, 2004) The second work was a characterization of two candidate reconstruction algorithms with specific emphasis on the recovery of absolute radiometric data. (Gustke, 2004)

Anatomy of the Sensor

Figure 3 contains a schematic of the CT. Dimensions labeled D_x represent the distances between objects and dimensions F_x represent lens focal lengths.
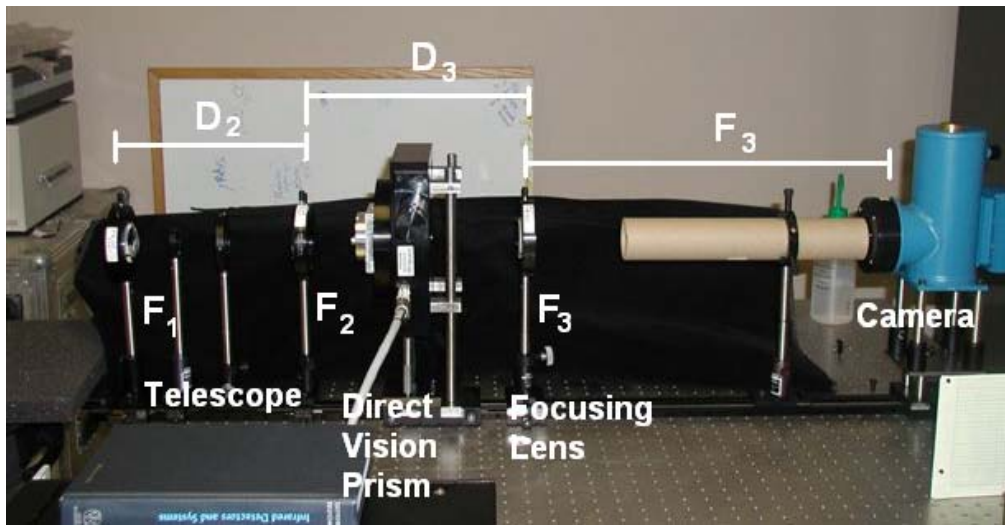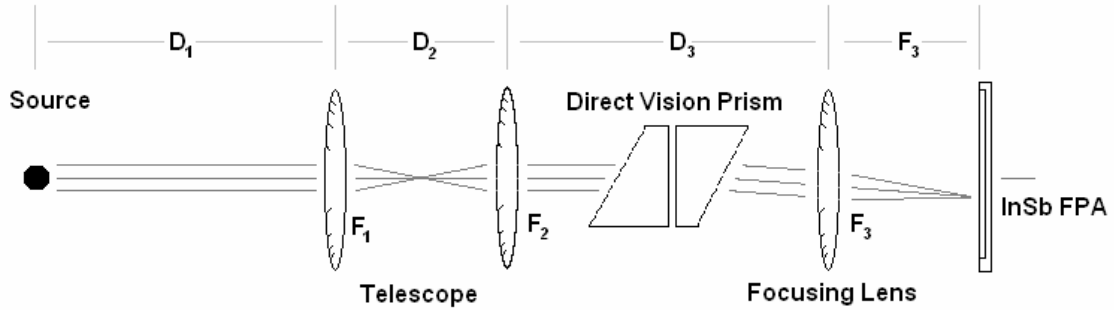
Figure 3. The CT System (Including Dimensions)

Moving from the source to the focal plane, a brief discussion of the components of the CT is in order before the parameters that govern them are described. The telescope has three primary purposes: to collimate the input, regulate image magnification, and

8

ensure that the signal is not interrupted by the edges of the direct vision prism system. After collimation, the signal enters the prism assembly where it is dispersed about some center wavelength according to its spectral content. During operation, the prism assembly rotates and so does the dispersed signal. As its name suggests, the focusing lens recreates the dispersed image of the source on the focal plane.

Prism Development

Constraints on the Direct Vision Prism.

Mr. Kevin Gross, a PhD candidate at AFIT, is the author of the original CT prism design in a collection of unpublished work. The following discussion is an expansion of his work, which included the development of prism design constraints and a survey of appropriate materials. Based on his conclusions, the fore prism (leftmost in figure 3) is best cut from Lithium Floride and the aft prism from Barium Floride. His original design called for a center wavelength at 3.61um, the center of the InSb bandpass, but this decision was made before it was known that the camera has a filter that narrows the bandpass down to 3-5 um. The proceeding discussion follows the development of the 4um center wavelength prism set designed to closely match the attributes of the original design. Aside from the enumeration of constraints, what follows is a completely independent development from Mr. Gross's original.

DVP Design Constrains

1) assembly must fit in a 2 inch diameter circular mount
2) undeviated wavelength should be 4um
3) undeviated wavelength should be tolerant of cut and alignment errors
4) dispersion should be monotonic over the 3-5um bandpass
5) useful aperture should exceed 25% of prism area
6) attenuation and reflection losses should be minimized
7) resolving power should be linear, or nearly so

9

Center Wavelength and Dispersion.

Understanding the behavior of radiation in the prism system is a prerequisite for understanding both the design criteria and, later, the wave optics model of the prism. Sellmeier index of refraction models for Barium Floride and Lithium Floride used throughout this research are taken from (Troph, 1995:1369).   Figure 4 is a diagram of the useful quantities in the following derivation.
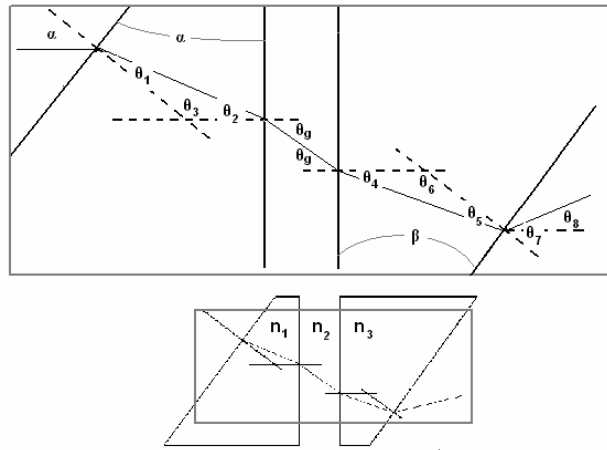
Figure 4. DVP Ray Trace Diagram

The smaller representation of the system identifies the relative location of the cutaway. θ_1 through θ_8 correspond to angles used throughout the derivation, α and β represent prism cut angles, and n_1 through n_3 represent the media specific index of refraction.

Radiation entering the DVP is collimated. The radiation path through the system is best expressed in terms of successive iterations of Snell's law.

$$\theta_1 = \sin^{-1}\left(\frac{n_1}{n_2}\sin\alpha\right) \tag{3.1}$$

10

$$\theta_2 = \alpha - \theta_1 \tag{3.2}$$

$$\theta_4 = \sin^{-1}\left(\frac{n_2}{n_3}\sin\theta_2\right) \tag{3.3}$$

$$\theta_5 = \beta - \theta_4 \tag{3.4}$$

$$\theta_7 = \sin^{-1}\left(\frac{n_3}{n_1}\sin\theta_5\right) \tag{3.5}$$

$$\theta_8 = \theta_7 - \beta \tag{3.6}$$

This result is valid with or without the presence of a gap between the prisms. If the gap is included

$$\theta_g = \sin^{-1}\left(\frac{n_2}{n_1}\sin\theta_2\right) \tag{3.7}$$

$$
\begin{aligned}
\theta_4 &= \sin^{-1}\left(\frac{n_1}{n_3}\sin\theta_g\right) = \sin^{-1}\left(\frac{n_1}{n_3}\sin\left(\sin^{-1}\left(\frac{n_2}{n_1}\sin\theta_2\right)\right)\right) \\
&= \sin^{-1}\left(\frac{n_1}{n_3}\frac{n_2}{n_1}\sin\theta_2\right) = \sin^{-1}\left(\frac{n_2}{n_3}\sin\theta_2\right)
\end{aligned}
\tag{3.8}
$$

hence equation 3.17 is identical to equation 3.12 and the rest of the derivation from 3.12 on continues unabated.

Sensitivity to Alignment Error.

The preceding development assumes that the two prism system is in perfect alignment though realistically this may not always be the case. Net alignment error can be expressed in terms of the effect along the axis of dispersion by modifying equations (3.4) and (3.6).

$$\theta_5 = \beta\cos\varphi - \theta_4 \tag{3.9}$$

11

$$\theta_8 = \theta_7 - \beta \cos\varphi \qquad (3.10)$$

where φ is the angular deviation from perfect alignment in terms of the aft prism.

Misalignment also gives rise to dispersion along the axis perpendicular to the axis of

intended dispersion. This off-axis dispersion, θ_{8p}, can be expressed as

$$\theta_{8p} = \sin^{-1}\left[\frac{n_3}{n_1} \sin\left(\beta \sin\varphi\right)\right] \qquad (3.11)$$

If θ_{8p} is ignored, misalignment can be interpreted as a shift in center wavelength.

Useable Aperture.

The left of figure 5 graphically depicts the regions 1 through 5 referred to in the

following development. Figure 5 on the right contains the end on view of the prisms.
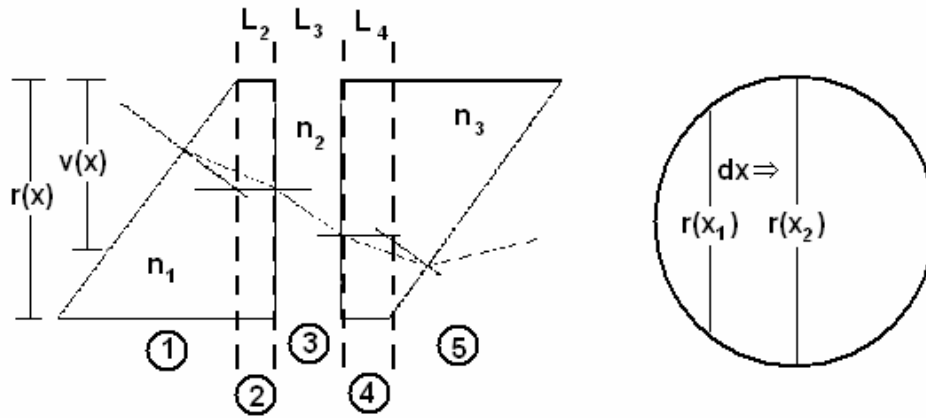
Figure 5. Regions of the Direct Vision Prism

The variable $r(x)$ represents the total prism height and $v(x)$ is the maximum ray

entrance height possible to avoid contact with the prism base. L_1 through L_3 represent

region widths. The prisms are circular therefore the values r and v, as depicted in the cross section shown in figure 5 are functions of x. r(x) is defined as

$$r(x) = r_{max} \sin\left(\pi \frac{x}{r_{max}} \right) \tag{3.12}$$

Dimension x is defined as distance from the left center of the prism cross-section.

The total drop, δ, from entrance to exit is expressed as the sum of the drops in each region.

$$\delta = (r(x) - v(x)) - v(x)\tan\alpha\tan\theta_2 - L_1\tan\theta_2 - L_2\tan\theta_g - L_3\tan\theta_4 \tag{3.13}$$

The value of v is determined by setting δ equal to zero and solving. Inspection of equation 3.17 reveals that δ is independent of β but not of n_3. In this context, percent useful aperture, UA, is defined as

$$UA = \frac{\int v(x)\cdot dx}{\int r(x)\cdot dx} \tag{3.14}$$

Note that the integral over r(x) is simply the surface area of the prism face. The angles specified in equation 3.19 are determined at a given wavelength. This wavelength should be selected to coincide with maximum dispersion if UA is to represent the region where all radiation across the bandpass is permitted to pass through the entire prism system without reflection.

Attenuation and Reflection Losses.

The radiation entering the prism is unpolarized. Transmittance across each interface can be expressed in terms of the Fresnel equations (Hecht, 2002:115-120)

13

$$Tr_{\perp}(\theta_i, \theta_t, n_i, n_t) = \left(\frac{n_t \cos\theta_t}{n_i \cos\theta_i} \right) \left(\frac{2\sin\theta_t \cos\theta_i}{\sin(\theta_i + \theta_t)} \right)^2 \qquad (3.15)$$

$$Tr_{=}(\theta_i, \theta_t, n_i, n_t) = \left(\frac{n_t \cos\theta_t}{n_i \cos\theta_i} \right) \left(\frac{2\sin\theta_t \cos\theta_i}{\sin(\theta_i + \theta_t)\cos(\theta_i - \theta_t)} \right)^2 \qquad (3.16)$$

In each case, θ_i and θ_t represent incident and transmitted angles and n_i - n_x represent the respective index of refraction. The subscripts on T_r represent the orientation of polarization (parallel and perpendicular). Total transmission through the prism system is given as

$$Tr(total) = \frac{\prod_4 Tr_{\perp}(\theta_i, \theta_t, n_i, n_t) + \prod_4 Tr_{=}(\theta_i, \theta_t, n_i, n_t)}{2} \qquad (3.17)$$

The index 4 represents the four interfaces encountered during propagation.

Resolving Power.

The sensor's ability to discriminate spectral features is an important attribute to understand. One possible measure of this ability is resolving power (Pedrotti, 1987:122)

$$R = \frac{\lambda}{(\Delta\lambda)_{min}} \qquad (3.18)$$

where λ represents wavelength and the denominator represents the minimum discernable distance (in terms of wavelength) between spectral features. Pedrotti's complete development is particular to a single prism specified by its apex angle and is therefore not appropriate for the direct vision prism though what follows is a development in the same spirit. The Rayleigh distance, the distance between the peak of the diffraction-limited point spread function and the first null serves as a gage for determination of R. The Rayleigh range (Pedrotti, 1987:335) is defined as

14

$$D_R(\lambda) = \frac{1.22 \cdot \lambda \cdot F_3}{h} \tag{3.19}$$

Note that each variable is defined as before. Using D_R, $(\Delta\lambda)_{min}$ can be expressed in the following terms

$$D_R(\lambda + \frac{\Delta\lambda_{min}}{2}) + D_R(\lambda - \frac{\Delta\lambda_{min}}{2}) = \frac{1.22 \cdot F_3}{h} 2\lambda \tag{3.20}$$

$$D_R(\lambda + \Delta\lambda_{min}) + D_R(\lambda - \Delta\lambda_{min}) \leq \left| F_3 \tan\theta_8(\lambda + \frac{\Delta\lambda_{min}}{2}) - F_3 \tan\theta_8(\lambda - \frac{\Delta\lambda_{min}}{2}) \right| \tag{3.21}$$

$$\frac{2.44\lambda}{h} \leq \left| \theta_8(\lambda + \frac{\Delta\lambda_{min}}{2}) - \theta_8(\lambda - \frac{\Delta\lambda_{min}}{2}) \right| \tag{3.22}$$

In this case, θ_8 is expressed as a function of λ and the small angle approximation for tangents is applied in equation 3.21. $(\Delta\lambda)_{min}$ is best determined numerically by representing $\theta_8(\lambda)$ as a third order polynomial.

There are two limits to the resolving power model. First, this definition ceases to have meaning if the point spread function falls entirely in one pixel on the focal plane array. Second, the results (as stated) are accurate only in the diffraction-limited case and hence this result is an absolute upper limit on resolving power.

Attributes of the Selected Prisms

Center Wavelength and Dispersion.

Figure 6 contains the direct vision prism dispersion angles with respect to wavelength for both the 3.61 um and 4.00 um center wavelength designs. The width of each curve represents the error associated with the manufacturer's prism cut tolerances (±30 arcsec). Dispersion over the 3 to 5 um band is not linear in either case but is monotonic. The total dispersion about the bandpass is less than 1 degree. The 4 um

15

curve is well described as a linear shift in wavelength from the 3.61 um curve, a property which manifests itself when calculating resolving power.
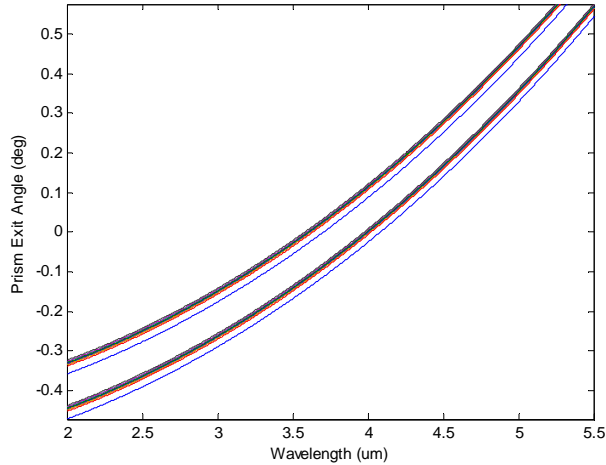
Figure 6. Direct Vision Prism Dispersion Angles

Curves representing a ±5° alignment error stand out to the right of the perfect alignment curves for each set of prisms. Though not shown on the plot, this error also produces an approximately constant shift of 0.03° along an axis perpendicular to the primary dispersion.

Useful Aperture.

Both prism systems exhibit a useful aperture of 92%, a result guaranteed by choosing the same material and cut angle for the leading prism. Figure 7 represents the concept of useful aperture graphically. In the plot, 5 um radiation, the wavelength of largest dispersion, is reflected off of the base of the prism assembly when it falls in the region between the r(x) and v(x) curves. This region of reflection forms a crescent along the edge of the leading prism at the base.

16
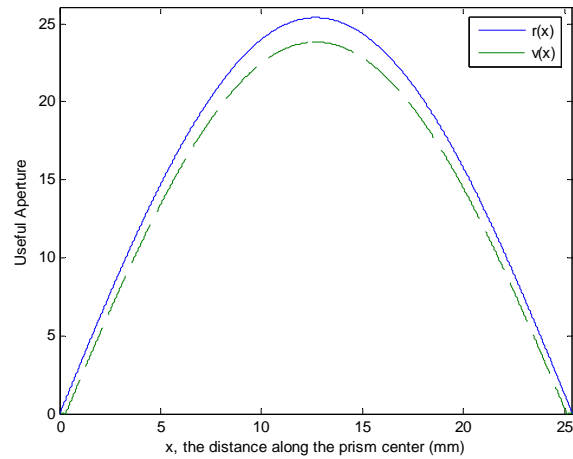
Figure 7. Graphical Representation of the Useful Aperture

Attenuation and Reflection Losses.

Total transmission through prism varies between 0.884 at 3 um to 0.900 at 5 um for both prism designs. Like the dispersion function, the transmission function is monotonic and otherwise unremarkable.

Resolving Power.

The plot in figure 8 shows that resolving power increases linearly with increasing wavelength. By inspection of equation (3.18), this result is an indication of constant spectral resolution over the prescribed bandpass. Though only one curve is plotted below, the resolving power results for both prism sets are virtually indistinguishable (as predicted in the previous discussion on dispersion).

17
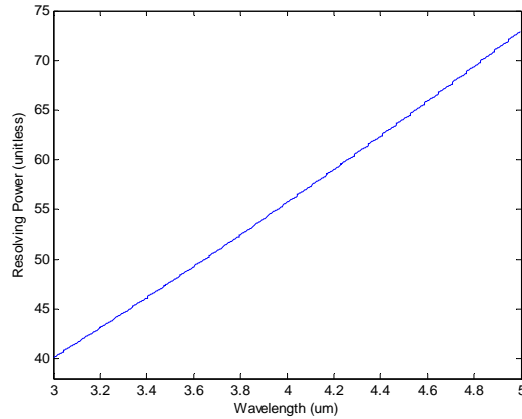
Figure 8. Resolving Power as a Function of Wavelength

Lens Development

Constraints on Lens Selection.

In general, lens selection constraints are restricted only what is required for

functionality. The fourth and fifth items in the following list of constraints are

constraints determined both by lens selection and by prism selection (refer ahead to

equation 3.8).

Lens Selection Constraints

1) lenses are selected from an array of 2 inch CaF lenses specified at f/1 through f/10
2) collimated light must pass through the DVP without interacting with the mount walls
3) field of view must be large enough to image a 1 inch diameter source
4) theoretical propagation theory predicted field of view should be maximized
5) image magnification must not result in signal falling off the focal plane
6) required bandwidth must fall entirely on the focal plane

18

Matrix Representation of the Optical System.

Ignoring the prisms for the moment, the transformation matrix of the system can be expressed as such using the following treatment. (Pedrotti, 1987: 70) Translations take the form

$$T(D_x) = \begin{bmatrix} 1 & D_x \\ 0 & 1 \end{bmatrix} \tag{3.23}$$

and the transformation at a lens interface is defined as

$$L(F_x) = \begin{bmatrix} 1 & 0 \\ -\dfrac{1}{F_x} & 1 \end{bmatrix} \tag{3.24}$$

In terms of these two components, the transformation of the system, M, can be defined as such

$$M = T(F_3) \cdot L(F_3) \cdot T(D_3) \cdot L(F_2) \cdot T(D_2) \cdot L(F_1) \cdot T(D_1) \tag{3.25}$$

The system defined by M will form an image on the focal plane when the following condition is satisfied

$$M_{12} = F_3 \frac{D_1(D_2 - F_1 - F_2) + F_1(F_2 - D_2)}{F_1 F_2} = 0 \tag{3.26}$$

where the subscripts on M represent the row and column position of the term in question. Equation 3.4 can be solved for D_2

$$D_2 = \frac{D_1 F_1 + D_1 F_2 - F_1 F_2}{D_1 - F_1} \tag{3.27}$$

19

Notice that, in the limit where D_1 goes to infinity, $D_2 = F_1 + F_2$, which is the expected result. Finally, we can establish the transverse magnification of the system by substituting this result for D_2 into M_{11}

$$M_{11} = -F_3 \frac{F_1 + F_2 - D_2}{F_1 F_2} = \frac{F_1 F_3}{D_1 F_2 - F_1 F_2} \tag{3.28}$$

Both the expressions for magnification and D_2 are completely independent of the distance D_3 and hence this dimension is discarded as a design constraint.

Field of View.

The field of view, θ_{fov} is an expression of the angular width of the scene captured on the FPA. Using similar triangles, the FOV can be expressed in terms of the linear width of the focal plane, W, and the effective focal length of the system

$$\theta_{FOV} = \tan^{-1}\left(\frac{w}{f_{eff}}\right) \tag{3.29}$$

If the entire optical system is modeled as a single thin lens, the effective focal length, f_{eff}, is given by manipulating the well known thin lens equation

$$\frac{1}{D_1} + \frac{1}{M_{11} D_1} = \frac{1}{f_{eff}} \tag{3.30}$$

Note that the effective focal length defined here is *not* the effective focal length associated with principal plane analysis, it is simply the calculated focal length of the system if it were modeled as a single thin lens located at the real position of the leading optic in the CT system. For now, the importance of f_{eff} can be summed up via the following expression for the Fresnel propagation region of validity (Goodman, 1996:69)

$$\left(f_{eff}\right)^3 >> \frac{\pi}{4\lambda}\left[\left(x - \xi\right)^2 + \left(y - \eta\right)^2\right] \tag{3.31}$$

20

where (x,y) and (ξ,η) represent the position in the image and object planes respectively. As later discussion will show, (3.31) may be overly restrictive but the advantage of maximizing f_{eff} is clear.

Determination of the Focal Lengths F_1 and F_2.

Ideally, the signal, once it has passed through the telescope, will have no interaction with the walls of the prism mount. The radiation from the source, under all conceivable operating conditions, can be considered nearly collimated at the aperture of the sensor. Under these conditions, the telescope is approximately afocal and the relationship between the diameter of the objective lens, H, and the diameter of its image (the exit pupil), h, can be approximated as follows (Hecht, 2002:221)

$$\frac{H}{h} = \frac{F_1}{F_2} \tag{3.32}$$

Assuming the conditions on the field of view are met, the problem of selecting F_1 and F_2 is therefore reduced to ensuring three things: h is less than the diameter of the useful prism aperture, the resulting system magnification is sustainable, and the effective focal length is as large as possible. Note that the last two requirements represent competing interests. Stray radiance from around the edges of the objective lens is prevented from entering the system via a stop placed between the lenses in the telescope. In this configuration, this stop serves as the field stop of the system.

Factors Influencing the Selection of the Focusing Lens.

The focusing lens defines both the magnification of the system from equation 3.6 and the linear dispersion of the image which, depending on the dimensions of the focal plane, can limit bandwidth. Given a prism exit angle, θ_8, the linear dispersion, L, at the focal plane is simply

$$L = F_3 \tan \theta_8 \tag{3.33}$$

Implicit in this expression is the counterintuitive requirement that neither D_3 nor the distance between the prism and the focusing lens affects the linear dispersion at the focal plane.

Under certain circumstances, pixel size will also effect the selection of F_3. Though it is clear from (3.22) that resolving power is not a function of F_3 in an analog sense, (3.19) shows that the width of the diffraction limited PSF is tied to F_3. In the limit where PSF's become small compared to pixel width, the definition of resolving power losses validity. This concern should be recognized in general but can otherwise be largely ignored because, as the results of this research will show, even the smallest PSF's have a width measurable over several pixels.

Transmission Losses in the Lenses.

Losses in the lenses are assumed to occur due to reflections at normal incidence at each of the six air/glass or glass/air interfaces. Transmittance at normal incidence is given by (Hecht, 2002:121)

$$Tr_n = \frac{4n_t n_i}{\left(n_t + n_i\right)^2} \tag{3.34}$$

22

where n_t and n_i represent the index of refraction of the incident and transmitted media. Since it is clear than transmittance at normal incidence is equivalent at both air/glass and glass/air interfaces, total transmittance through three lenses is given by the sixth power of Tr_n. These losses are insubstantial, unavoidable and are not necessary as part of the design process.

Attributes of the Selected Lenses

Telescope Lens Selection.

As stated in the constraints, lens selection must be placed in the context of the selected prisms. The direct vision prism system has a diameter of 25 mm and a useful aperture of approximately 91%. By equation (3.32), the ideal ratio of F_1 to F_2 would be slightly less than 2.1 to fully utilize the useful aperture though prism interior reflections will result if this ratio is reduced further. A ratio of 2.5 is attainable using the f/3 and f/2 lens combination as is ratio of 3 using an f/3 and f/1 combination. Of the two choices, effective focal length receives a boost by choosing the f/3 – f/1 combination. Consequently, the f/3 (15.24 cm focal length) and f/1 (5.08 cm focal length) combination is selected to be the best compromise.

Focusing Lens Selection.

There are four primary factors that influence the selection of F_3: bandwidth, magnification, effective focal length and field of view. The results of the angular dispersion plot in figure 6 combined with equation (3.33) shows that the total linear dispersion between 3 to 5 um on the focal plane will cover 228 pixels (each pixel is 24 um wide) using the f/10 lens. The entire focal plane has dimensions of 640 by 512

23

pixels therefore, even in the most extreme case, selection of focal length F_3 will not restrict the desired bandwidth.

   Effective focal length and total magnification both increase with an increase in F_3. The case for increasing f_{eff} has already been made but field of view must be kept in check to prevent portions of the incident signal critical to PSF extraction from leaking off the focal plane. The source described in lens selection criteria only requires a field of view of 0.33° if it were imaged perfectly but aberrations expand this requirement significantly. Based on the comparison in table 2 and with this restriction in mind, the f/5 lens (25.4 cm focal length) is best suited for this research.

Summary of Selection Results

   Tables 3 and 4 summarize the selection of optical components and their attributes. Aside from center wavelength, the attributes of both prism designs are virtually indistinguishable. Though interesting, this result is not necessarily surprising because the center wavelength change was implemented by only a small change in the Barium Floride prism cut angle. For comparison, several results for the f/10 focusing lens are also included.

Table 1. Specifications of the Direct Vision Prism

Center λ (um)	angle α	angle β	Total Dispersion	UA	Transmission (%)	Resolving Power
3.61	18°33'06"	14°34'30"	-0.16° to 0.46°	0.92	0.88 to 0.90	40 to 73 (linear)
4.00	18°33'06"	14°20'34"	-0.26° to 0.35°	0.92	0.88 to 0.90	40 to 73(linear)

The total dispersion defined in table 1 is in terms of the 3 to 5 um bandpass. The two prism systems are, in terms of most figures of merit, identical.

Table 2. Lens System Specifications

F_1 (cm)	F_2 (cm)	F_3 (cm)	D_1 (cm)	D_2 (cm)	Magnification	F effective (cm)	FOV (deg)
15.24	5.08	25.40	434.34	20.87	0.18	66.82	0.81
15.24	5.08	50.80	434.34	20.87	0.36	115.82	0.55

The first row of table 2 contains the specifications of lenses used during this research, the second row exists for the sake of comparison.

Assembly and Alignment of the Direct Vision Prism System

DVP Assembly.

Material considerations complicate what would otherwise be the simple task of coupling and mounting the direct vision prisms. According to the prisms' manufacturer, optically bonding the Barium Floride and Lithium Floride prisms is possible, but no adhesive is available with favorable transmission properties in the mid-wave IR. Furthermore, holding the two prisms together with a heat activated shrink wrap is also impossible because Barium Floride is extremely sensitive to thermal shock. As a result, the two prisms are separately mounted mechanically and then attached and aligned. Figure 9 shows the prisms in their mounts, coupled together, and attached to the rotation stage.

25
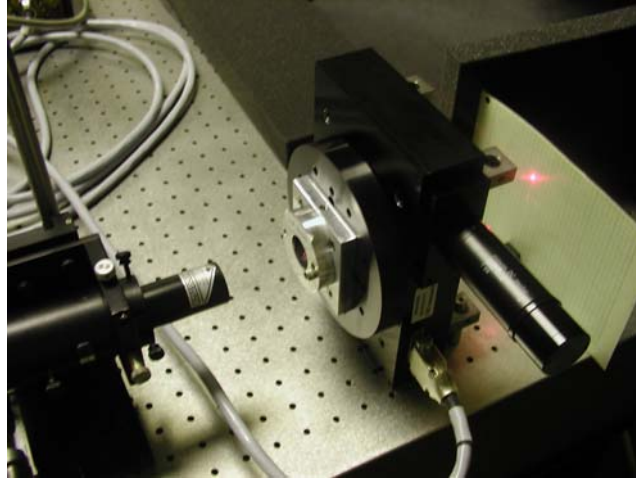
Figure 9. The Direct Vision Prism Assembly

The fore prism mount (Lithium Floride) consists of a cylindrical section of machined aluminum with a concentric inner ring cut to hold the prism. The prism is wrapped in an adhesive backed neoprene sheath and held against a lip facing the aft prism section. The sheath is necessary to prevent chipping at the glass-aluminum interface (a lesson learned). A set screw is used to secure the wrapped prism in place. This mount is held to the aft prism mount via a bolt in a hole that sweeps out a 10° arc for alignment purposes.

The aft prism mount also contains a circular hole and set screw system to contain the prism and hold it against a lip facing the fore prism mount. This mount bolts directly to the rotation stage. To aid the explanation, figure 10 contains a diagram of the two mounts.

المنارة للاستشارات

www.manaraa.com
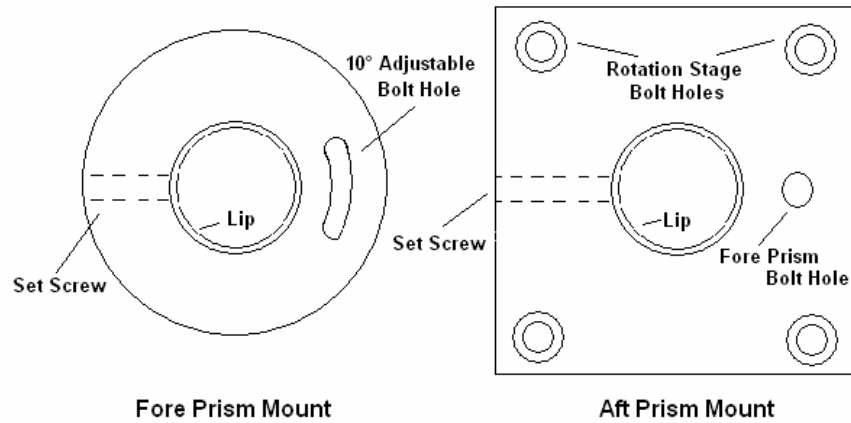
Figure 10. Schematic of the Prism Mounts

The two lips create a net air gap between the two prisms of 0.16 cm. The presence of the air gap prevents the two prisms from rubbing during alignment but also reduces the useful aperture (the calculations in table 1 include this gap).

DVP Alignment.

Inspection of the geometry in figure 3 indicates that, when the prisms are perfectly aligned, both reflections and transmissions through the prisms will occur in the plane whose normal is perpendicular to the optical axis. Analytically, this statement is reinforced by the development for φ in the previous discussion of alignment errors. A NeHe pointing laser, shown in figure 9, is used to exploit this relationship for alignment purposes. Proper alignment is achieved when two points of reflection, captured on a paper screen facing the fore prism assembly, and two points of transmission, captured on a screen facing the aft assembly, all fall in the expected plane. Alignment deviations show up as a rotation out of this plane away from the optic axis normal. Figure 9 shows the bright primary transmission point and a dim secondary reflection dot lined up on the aft prism facing screen.

27

IV. The Fourier Transform Propagation Model

Each simulated broadband image is formed as a summation of many monochromatic images. In turn, these monochromatic images are formed as a convolution of the geometrically predicted image of the source with a point spread function specific to the sensor. The following development explains how these point spread functions are derived and applied for the ultimate purpose of image formation.

Propagation Theory Fundamentals

Fresnel Propagation.

The following expression relates the field in the image plane to the field in the object plane using the Fresnel propagation integral. (Goodman, 1995:67)

$$U(x,y) = \frac{e^{\frac{j2\pi z}{\lambda}}}{j\lambda z} e^{\frac{j\pi}{\lambda z}(x^2+y^2)} \int_{-\infty}^{\infty} \int_{-\infty}^{\infty} \left[U(\xi,\eta) e^{\frac{j\pi}{\lambda z}(\xi^2+\eta^2)} \right] e^{\frac{j\pi}{\lambda z}(\xi x+\eta y)} d\xi d\eta \tag{4.1}$$

where $U(x,y)$ and $U(\xi,\eta)$ represent the field in the image and object planes and, for purposes of simplicity, each field has units of the square root of intensity $(\sqrt{Watts}/cm)$. The variable z in (4.1) represents the distance between the planes described by (x,y) and (ξ,η). By applying the following change of variables:

$$f_x = \frac{x}{\lambda z}$$
$$f_y = \frac{y}{\lambda z} \tag{4.2}$$

the Fresnel integral can be transformed into a scaled Fourier transform

$$U(x,y) = \frac{e^{\frac{j2\pi z}{\lambda}}}{j\lambda z} e^{j\pi\lambda z(f_x^2+f_y^2)} \mathcal{F} \left\{ U(\xi,\eta) e^{\frac{j\pi}{\lambda z}(\xi^2+\eta^2)} \right\} \tag{4.3}$$

28

where the script F represents the Fourier transform operator. In both cases, the corresponding intensity pattern is given by

$$I(x, y) = U(x, y)U^*(x, y) \qquad (4.4)$$

Multiplication by the conjugate annihilates the effects of any constant phase terms. Consequently, it is often convenient to drop these terms early on during computation to simplify bookkeeping.

Two Essential Properties of the Fresnel Propagation.

A limit on the validity of Fresnel propagation was imposed earlier in equation (3.31) in terms of the effective focal length. In general, this equation can be recast in terms of z but, as explained in the reference (Goodman, 1996:69), this limit does not apply in all cases. As a result, quantifying the region in the image plane where the Fresnel approximation applies in difficult to determine in the absence of system specific measurements. Any number of separate Fresnel regions could be defined for the focal plane of the CT system but this is a task best left to a future thesis. Assuming the images made by the CT fall into a single one of these regions, the following statements define a system a properties shared by every included intensity pattern. Except where specifically noted, reference for these properties can be found in chapter 2 of the Goodman text.

Invariance.

An optical system is considered to be temporally and spatially invariant if the only result of a change in an object's position is a change in its image. Note that this definition applies specifically to the *optical system* but makes no reference to a source, which may or may not be invariant. This is a property shared by both Fresnel and geometric propagation. Put another way, if I(x,y) is the image formed from an object

29

described by $I(\xi,\eta)$ and a is a proportionality constant that links one coordinate system to the other then for a space invariant system

$$I(\xi,\eta) \otimes \delta(\xi-\xi_0, \eta-\eta_0) \xrightarrow{\text{Propagation}} I(x,y) \otimes \delta(x-a\xi_0, x-a\eta_0) \qquad (4.5)$$

where $\xi 0$ and $\eta 0$ represent the position of the center of the shifted object intensity pattern and δ symbolizes the Dirac delta function. Though the reasons why are not explicitly laid out in equation (4.5), this property will be critical to the development of the prism transformation phase screen.

Linearity.

A generic linear operator, S, exhibits the following properties in all cases

$$S\{u \cdot I_1(x,y) + v \cdot I_2(x,y)\} = u \cdot S\{I_1(x,y)\} + v \cdot S\{I_2(x,y)\} \qquad (4.6)$$

where u and v are scalar modifiers of intensity patterns I_1 and I_2. The operator S could represent the Fresnel propagation itself (which leads directly to the following property) or S could represent a pattern summing operator which allows for the superposition of intensity patterns to form a single image. Consequently, this property can be used to describe a polychromic intensity pattern as a composite of many individual monochromatic patterns.

Image Formation as a Convolution

The image formed by a linear invariant optical system can be expressed as a convolution of the system specific impulse response (point spread function) and the geometrically predicted image of the source. (Goodman, 1995: 21)

$$I(x,y) = s(x,y) \otimes g(x,y) \qquad (4.7)$$

where s(x,y) is the normalized intensity pattern of the point spread function and g(x,y) is the geometric intensity pattern of the source.

Calculation of g(x,y) is straightforward if the origins of both image plane (x,y) and the object plane (ξ,η) are defined to lie on the optical axis.

$$g(x, y) = g(\frac{\xi}{M_{11}}, \frac{\eta}{M_{11}}) \tag{4.8}$$

where M_{11} is the magnification defined in (3.28). This expression has nothing to do with Fresnel propagation; it is simply a mapping from one plane to the other.

Calculating the Point Spread Function

Physically, the point spread function is formed as the image of a unit intensity point object. Analytically, this field corresponding to the point object at the aperture, $Ap(\xi,\eta)$, that has the following property

$$\int_{-\infty}^{\infty} \int_{-\infty}^{\infty} Ap(\xi, \eta) \cdot Ap(\xi, \eta)^* d\xi d\eta = 1 \tag{4.9}$$

Equation (4.9) states that the aperture must have a finite area but places no restrictions on the dimensions of that area. Furthermore, this definition places no restrictions on the phase at the aperture (which includes atmospheric aberrations induced during propagation). Regardless of the size of the aperture, the total intensity collected is normalized to 1.

A lens is required to form the image. The function form of a thin lens is taken to be (Goodman, 1995:99)

$$t_1(\xi, \eta) = e^{-\frac{j\pi}{\lambda f}(\xi^2 + \eta^2)} \tag{4.10}$$

31

where f is the effective focal length of the lens. This phase model is adequate to form a theoretical image but real images include lens aberrations which requires the addition of another phase term (Roggemann, 1996:27)

$$t_{ab}(\xi, \eta) = e^{\frac{j\pi}{\lambda}\gamma(\xi,\eta)}$$ (4.11)

where $\gamma(\xi,\eta)$ is a measurement of the phase aberrations at every point in the pupil, presented in terms of wavelengths. This aberration function can be build as linear combination of individual aberrations using Zernike polynomials (Roggemann, 1996:95) or they can be sampled from the optical system itself (a process which is demonstrated in this research). t_{ab} can also be used to represent near field atmospheric aberrations that occur during propagation through space. For brevity sake, all lens transformations will henceforth be expressed as a combination of the thin lens and aberration transformations.

$$t(\xi, \eta) = e^{-\frac{j\pi}{\lambda f}(\xi^2+\eta^2)} e^{\frac{j\pi}{\lambda}\gamma(\xi,\eta)}$$ (4.12)

All the tools required to form the point spread function are now in place. Referring back to (4.3) the field produced in the focal plane due to the point object is given to be

$$U_{PSF}(x, y) = \frac{e^{\frac{j2\pi z}{\lambda}}}{j\lambda z} e^{j\pi\lambda z(f_x^2+f_y^2)} \mathcal{F}\left\{Ap(\xi, \eta) t(\xi, \eta) e^{\frac{j\pi}{\lambda z}(\xi^2+\eta^2)}\right\}$$ (4.13)

Completely expanded, two of the exponential terms cancel because, for focused image formation z must equal f, and the equation reduces to

$$U_{PSF}(x, y) = \frac{e^{\frac{j2\pi z}{\lambda}}}{j\lambda z} e^{j\pi\lambda z(f_x^2+f_y^2)} \mathcal{F}\left\{Ap(\xi, \eta) e^{\frac{j\pi}{\lambda}\gamma(\xi,\eta)}\right\}$$ (4.14)

32

and hence the point spread function intensity pattern is given by

$$s(x, y) = U_{PSF}(x, y)U_{PSF}^{*}(x, y) \qquad (4.15)$$

A Single Lens Phase Model

At first glance, it appears that at least four Fresnel propagations are necessary to model the CT optical system since there are three separate lenses between the source and the focal plane. A multi-propagation approach will yield the correct result but the system is greatly simplified by the constraint that radiation entering the direct vision prism is collimated (or nearly so). This constraint is manifest in equation (3.25) where the distance between lens F_3 is set to be the length F_3.

If the edge effects of the optics in the interval are approximately nil, the source can be considered to be an aberrated plane wave incident on the focusing lens. These aberrations are picked up in the atmosphere, in the telescope portion of the optical system, and in the prisms, but, as long as they are represented adequately (sampled properly), they need not be considered separately. Of course, the efficacy of this approximation is dependent upon the acceptability of its effect on the results.

As stated previously, this approximation is not absolutely necessary but it is preferable for two reasons. The first (and lesser) reason is computational simplicity; the number of Fourier Transforms required for a given propagation is reduced from one for each optical interface to a total of one. Second, while it is possible to measure the effects of aberrations separately in each optical element, unless perfect alignment is achieved, the net effect of these aberrations is not equal to the sum of its parts. Treating the all aberrations as an event in a single plane and making corresponding measurements accounts for both optical imperfections and alignment errors while approximating out the

33

edge effects of the intervening optics. Making measurements of these aberrations is the subject of the proceeding chapter.

Definition of the Aperture Function.

The field associated with collimated light is described analytically in terms of a plane wave. Furthermore, the collimated beam at the exit of the telescope has a diameter h as defined in equation (3.32). In terms of plane waves alone, the normalized aperture function is defined as

$$\mathrm{Ap}_{\mathrm{plane}}(x_3, y_3) = \begin{cases} \dfrac{e^{\frac{j2\pi D_3}{\lambda}}}{\pi\left(\frac{h}{2}\right)^2} & \sqrt{x_3{}^2 + y_3{}^2} \le h \\ 0 & \sqrt{x_3{}^2 + y_3{}^2} > h \end{cases} \tag{4.16}$$

where (x_3, y_3) are the coordinates in the plane of the lens F_3. Note that the constant phase term in this equation does depend on D_3 but, as stated previously, constant phase is of no consequence in terms of intensity. The value of h corresponds to the radius of the aperture.

Aberrations introduced into the signal due to atmosphere and imperfect telescope optics are lumped together as a virtual thin lens applied to the system in the plane of propagation. These aberrations combined with the previous result form the field at the entrance of the focusing lens

$$\mathrm{Ap}(x_3, y_3) = \mathrm{Ap}_{\mathrm{plane}}(S_c x_3, S_c y_3) e^{\frac{j\pi}{\lambda} S_c \gamma_{\mathrm{prop}}(x_3, y_3)} \tag{4.17}$$

where γ_{prop} is the atmosphere and telescope aberration phase screen and S_c is a wavelength scaling factor that will be described in the next section.

Physical Manifestation of γ_{prop}.

A brief digression is useful at this point to provide context for equation (4.17). If $\gamma_{prop}(x_3, y_3)$ were set to zero at all points and the subsequent aperture function substituted into the transformation in (4.14), the resulting field at the focal plane (see figure 11) would be the familiar Airy pattern, the diffraction limited point spread function.
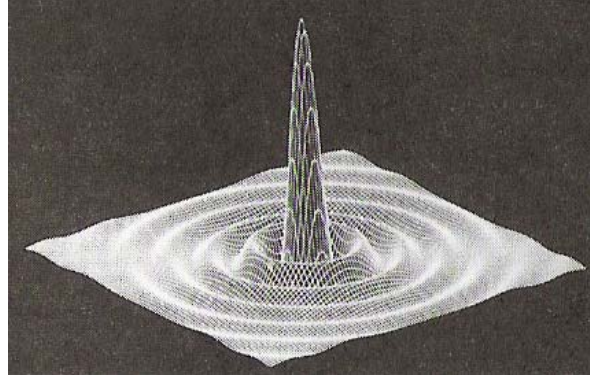
Figure 11. The Diffraction Limited PSF (Hecht, 2002:469)

In cases where $\gamma_{prop}(x_3, y_3)$ is not zero over all space, the convolution property of the Fourier transform is applied (Goodman, 1996:9).

$$\mathscr{F}\left\{Ap_{plane}e^{\frac{j\pi}{\lambda}\gamma_{prop}}\right\} = \mathscr{F}\left\{Ap_{plane}\right\} \otimes \mathscr{F}\left\{e^{\frac{j\pi}{\lambda}S_c\gamma_{prop}}\right\} \qquad (4.18)$$

Hence the field in the focal plane can be interpreted as the convolution of the Airy disk with the transform of the aberrations accumulated along the optical path.

The phase screen γ_{prop} is measured at a single wavelength at a given aperture size. The magnitude of the aberration is achromatic therefore a scaling factor is introduced into the exponent so that the phase measurements can be applied to all wavelengths of interest.

35

$$S_c = \frac{\lambda}{\lambda_m} \qquad (4.19)$$

where λ is the wavelength of propagation and λ_m is the wavelength where the phase screen was initially measured. The similarity theorem of the Fourier transform

$$\mathcal{F}\{g(S_c x, S_c y)\} = \frac{1}{S_c^2} G\left(\frac{f_x}{S_c}, \frac{f_y}{S_c}\right) \qquad (4.20)$$

demonstrates that the effect of this scaling, besides normalizing the phase screen, is to scale the result of the transform in image space by the inverse of the scale factor. The physical implication of this result is that the PSF will be wider for longer wavelengths and more narrow for shorter wavelengths. This contraction and expansion is verified independently by the definition of the Rayleigh Criterion in equation (3.19).

The Direct Vision Prism

Up to this point, no consideration has been given to the effects of the direct vision prism on the model. Recall from equation (4.5) the requirement for spatial invariance in the image plane. Under this regime, the effect of the prism must be to shift the image (and by logical extension, the PSF) but leave it otherwise completely intact. The effect on the PSF due to the prism in the image plane is

$$U'_{PSF} = U_{PSF} \otimes \delta(x - u, y - v) \qquad (4.21)$$

where u and v represent linear dispersion in the image plane. The variables u and v share the following relationship with equation (3.33)

$$\begin{aligned} u &= F_3 \tan \theta_{8p} \\ v &= F_3 \tan \theta_8 \end{aligned} \qquad (4.22)$$

36

The effects of dispersion are brought back into the diffraction plane (ξ,η) by the inverse Fourier transform of (4.21).

$$\mathcal{F}^{-1}\left\{U'_{PSF}\right\} = Ap_{plane}e^{\frac{j\pi}{\lambda}S_c\gamma_{prop}}e^{\frac{j2\pi}{\lambda}\left(\xi\tan\theta_{8p}+\eta\tan\theta_8\right)} \qquad (4.23)$$

In terms of phase, the prism is manifests itself as an additional aberration term in the plane of diffraction.

The Discrete Direct Vision Prism Transformation.

The preceding derivation expresses all transformations in terms of continuous functions. With the exception of the prism transformation, the continuous case migrates into the discrete case with relative ease, assuming that specific sampling requirements are met (see the following section on sampling). The discrete prism transformation is analogous to its continuous counterpart but sufficiently different the two warrant some specific attention.

The circular shift property of the DFT (Strum, 1989:399) is expressed in one dimension as

$$D\left\{g(k)e^{\frac{j2\pi}{N}km}\right\} = G(n \oplus m) \qquad (4.24)$$

where D is the DFT operator, $g(n)$ is the transformation of $G(k)$, N is the number of samples in the array, and m is the specified shift. For this application, m corresponds to the direction and magnitude of the linear dispersion in a particular direction

$$m = \frac{u}{dx} \quad (off-axis)$$
$$\qquad\qquad\qquad\qquad (4.25)$$
$$m = \frac{v}{dx} \quad (on-axis)$$

where u and v come from the development in (4.22) and dx is the sampling distance in the image plane. Consequently, equation (4.23) can be recast in discrete space as

$$\mathbf{D}^{\prime}\left\{U^{\prime}_{PSF}(n_1, n_2)\right\} = Ap_{plane}(k_1, k_2)e^{\frac{j\pi}{\lambda}S_c\gamma_{prop}}e^{\frac{j2\pi}{N}\left(\frac{k_1F_3\tan\theta_{8P}}{dx} + \frac{k_2F_3\tan\theta_8}{dx}\right)} \tag{4.26}$$

where the indices n_x and k_x represent the sampled versions of the corresponding functions. At this point, the parallel between (4.23) and (4.26) is obvious.

Formation of the Composite Image and Radiometry

Equation (4.26) rounds out all of the required steps necessary to generate a point spread function for any wavelength of interest. Additionally, the discrete version of equation (4.7) provides the mechanism necessary to apply the PSF to the problem of real image formation. What remains then is to combine these results to form a complete polychromatic image by appropriately scaling the intensity in terms of wavelength and summing the resulting intensity patterns.

Scaling with Intensity.

In terms of the geometrically predicted image, the total power per unit wavelength incident on the focal plane, $P(\lambda)$, is given by

$$P(\lambda) = \sum\sum g(\xi, \eta)\Delta\xi\Delta\eta \tag{4.27}$$

where $\Delta\xi\Delta\eta$ is the area of a pixel in the focal plane and g is defined as in equation (4.8). This equation provides a simple mechanism for ensuring that the correct amount of power is deposited on each pixel in terms of each wavelength of interest. Throughout this research the source is a circular cavity blackbody of temperature T. The problem remains then to define power per unit wavelength incident on the focal plane:

38

$$P(\lambda) = \left(\frac{L_{bb}(\lambda, T) A_s A_o}{D_l^2} \right) T_f T_c T_w T_a T_{CaF} \qquad (4.28)$$

where the term in parentheses is a measure of the total power from a source (of area A_s) collected by the leading optic of the system (area A_o) over a distance of D_l. The term T_x represent the various mediums and filters though which the radiation must pass. In order of appearance from left to right these absorbers include:

Tf   a source filter (set to 1 for broadband sources)
Tc   transmission through the camera cold filter
Tw   transmission through the camera window
Ta   transmission through the atmosphere (Modtran)
TCaF   transmission through the three Calcium Floride Lenses

Each of these transmission terms deserves some discussion but first all qualms about lumping these terms together must be laid to rest. Recall from the discussion of linearity of the Fourier transform that constant terms, in this case the magnitude of the electric field or one of its modifiers, may be pulled out of each transformation and considered separately. As a result, the magnitude electric field at the image plane (and hence the total power) need only to be calculated once as the product of the propagated field and its modifiers, which, in this case are the various absorbers.

All sources suffer the effects of the last five absorbers mentioned above. Data on T_c and T_w is taken from the camera manufacturers documentation (SBFP, unk:13-54) and transmission through the Calcium Floride lenses comes from the treatment in equation (3.34) along with the subsequent discussion.

Approximation of the transmission through the atmosphere was determined using Modtran4's standard US atmospheric model at constant pressure with a path length of 5

meters. The actual path length from source to FPA is slightly less than this distance but

Modtran4 does not support path length increments of less than 1 meter. For more

information on Modtran4 see (Berk, 2003).

Rounding out equation (4.28), $L_{bb}(\lambda,T)$ represents blackbody photon radiance of

the source (Dereniak,1996:66)

$$L_{bb}(\lambda, T) = \frac{2c}{\lambda^4 \left(e^{\frac{hc}{\lambda kT}} - 1 \right)} \tag{4.29}$$

where h is Planck's constant, c is the speed of light, and k is Boltzman's constant.

A typical example of $P(\lambda)$ for a blackbody source at 400°C is given in figure 12

for the 3 to 5 um bandpass.
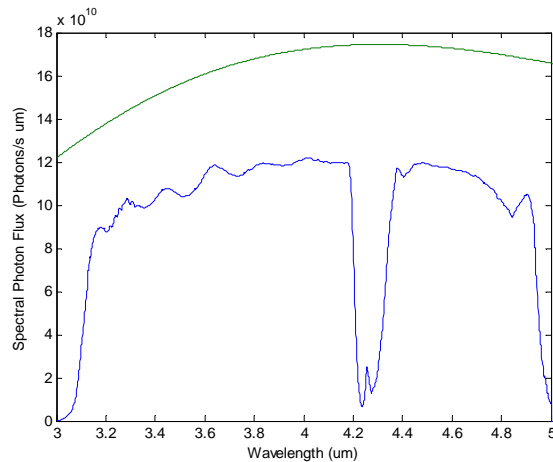

Figure 12. Blackbody Spectral Flux at the Focal Plane

The upper (smooth) curve represents the total photon flux in the absence of absorbers and is

provided as a reference. The lower curve is the flux used to approximate $P(\lambda)$ in the simulation.

Notice the prominent atmospheric feature found near 4.3 um. The edges of the bandpass a

defined primarily by the cold stop filter.

40

Summing Intensity Patterns.

The second issue is also easily resolved. By definition this optical system is
linear in intensity. As a result, a polychromatic image can be expressed as a sum of many
(approximately) monochromatic images assuming that the image is sampled
appropriately in wavelength. The Nyquist sampling theorem (Strum, 1988:54)
guarantees that the analog polychromatic signal can be recovered so long as the sampling
frequency, f_s, meets the following criterion:

$$f_s > 2f_{max} \qquad\qquad (4.30)$$

where f_{max} is the zero amplitude cutoff frequency of the power spectrum. Note that the
power spectrum is the Fourier transform of $P(\lambda)$. In practice, a zero amplitude frequency
may not exist but can be approximated by selecting the cutoff where the amplitude is
several orders of magnitude lower that the peak. Figure 13 contains a plot of the Fourier
transform of $P(\lambda)$ for both a simple blackbody at 400°C (the smooth curve) and the
blackbody modified by the aforementioned absorbers. As a reference, 10 um-1 can be
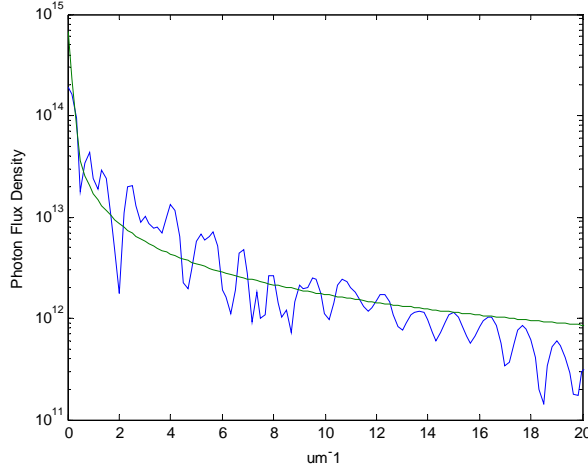considered an adequate cutoff for sampling purposes.

41

Figure 13. Fourier Transform of the Blackbody Spectrum

Given this cutoff, f_s must be at least 20 um^{-1} and hence sampling should occur at 0.05 um intervals.

Prism Rotation

The rotation of the direct vision prism can be handled in one of two ways depending on the geometry of the source. For circularly symmetric sources, such as the blackbody source used in this research, prism rotation can be applied directly to the composite intensity pattern, I(x,y), using the following transformation matrix

$$\begin{bmatrix} x' \\ y' \end{bmatrix} = \begin{bmatrix} \cos\theta_{rot} & \sin\theta_{rot} \\ -\sin\theta_{rot} & \cos\theta_{rot} \end{bmatrix} \begin{bmatrix} x \\ y \end{bmatrix} \tag{4.31}$$

where θ_{rot} is the prism rotation angle measured counterclockwise from the line x = 0.

Most sources in nature will not be circularly symmetric. In these cases, the transformation in (4.31) should be applied directly to the prism phase screen before it is multiplied with the aberration phase screen. This approach is also suitable for circular sources but much less efficient.

42

The previous section discusses the application of γ_{prop} but the problem of deriving γ_{prop} remains. First, a concise explanation of what the phase screen does and does not contain is appropriate. Recall that γ_{prop} describes the diffraction plane field phase of the on-axis space and time invariant point spread function. Consequently, γ_{prop} is independent of the source. Additionally, no mention has been given to the field effects of the prism assembly; the screen is intended to capture only the effects of aberrations caused by lenses and their alignment. Given these restrictions, the first task is to extract the point spread function from measurements made in the laboratory.

True monochromatic point sources, which are required for a direct measurement of the point spread function, are difficult to fabricate in the laboratory. To circumvent this problem, the Richardson-Lucy algorithm is applied to a measurement of a (nearly) monochromatic source with known spatial dimensions to statistically estimate a PSF at the center wavelength.   To generalize the PSF to all wavelengths, a second algorithm is then applied to extract the phase.

The Richardson-Lucy Algorithm

The Richardson-Lucy algorithm (Lanteri, 1972:55) addresses the problem of recovering an original image from its degraded measurement. In Lanteri's parlance, the relationship between the two is given as

$$f(x, y) = g(x, y) \otimes h(x, y) \tag{5.1}$$

where f is the degraded image, g is the original image, and h is the point spread function. Consequently, the problem of recovering g amounts to a deconvolution. Given f(x,y) and h(x,y), the Richardson-Lucy algorithm suggests an iterative approach to this problem:

43

$$g_{k+1}(x,y) = g_k(x,y) \cdot h^*(-x,-y) \otimes \frac{f(x,y)}{h(x,y) \otimes g_k(x,y)} \qquad (5.2)$$

where k is the index of iteration and $g_0(x,y)$, the initial guess, is constant, positive, and normalized.

Without appropriate modification, the Richardson-Lucy algorithm does not provide a mechanism for calculating h(x,y), which is the stated goal. As an intermediate step, the commutative property of convolution must be invoked

$$f(x,y) = h(x,y) \otimes g(x,y) \qquad (5.3)$$

and the Richardson-Lucy algorithm is recast as

$$h_{k+1}(x,y) = h_k(x,y) \cdot g^*(-x,-y) \otimes \frac{f(x,y)}{g(x,y) \otimes h_k(x,y)} \qquad (5.4)$$

which is an iterative solution for estimating the point spread function given the original image and its corresponding measurement. As an aside, note that equation (5.3) is identical to equation (4.7).

Source Setup.

The RL algorithm for calculating h(x,y) requires as input both the perfect (ray traced) image of a source, g(x,y), and a measurement of the monochromatic source image though the optics, f(x,y). A monochromatic source is approximated in the lab using a blackbody coupled with a narrowband thin-film filter. Figure 14 contains the measurement of this particular filter's response made using a Bomem MR-254 FTIR spectrometer. Radiation passing through the filter will fall predominantly between 4.2 and 4.4 um.
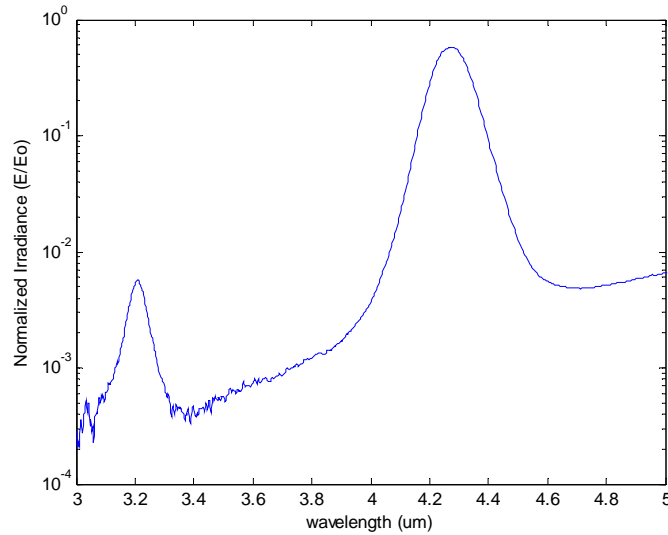
44

Figure 14. Filtered Blackbody Irradiance, Normalized to the Unfiltered Response

Sampling Issues.

Like the wavelength sampling issues discussed in chapter 4, similar issues must also be addressed here in two dimensions. The ultimate goal is to adequately sample the point spread function which, by extension, requires that both $g(x,y)$ and $f(x,y)$ are sampled correctly. The pixel size in the focal plane determines the sampling in $f(x,y)$ and is therefore also a convenient sample size to choose for $g(x,y)$. To test if this sample size is adequate, the Fourier transform of both $g(x,y)$ and $f(x,y)$ are examined to ensure that a reasonable cutoff frequency is reached. Figure 15 contains a measurement of $f(x,y)$ (left) and its Fourier Transform (right).

45
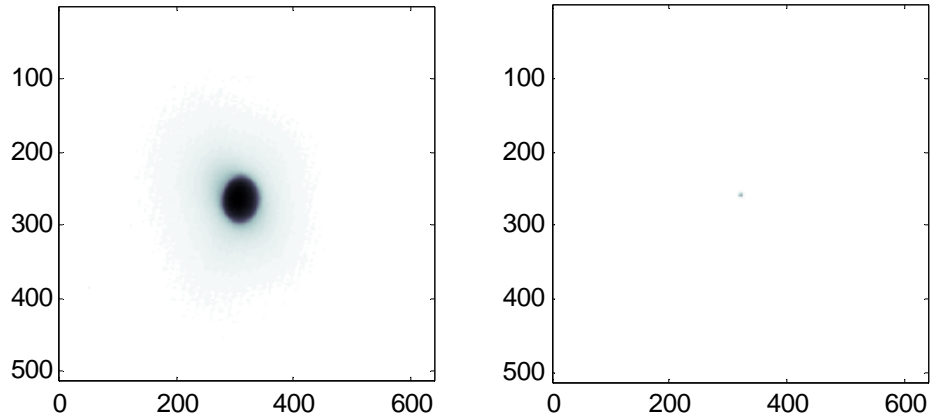
Figure 15. A Captured Image f(x,y) and its Fourier Transform

The image is of a filtered, circular blackbody source of diameter 1.02 cm formed as the average of 15 frames taken at 72 Hz. The background (due to internal reflections and emission along the optical path) is suppressed and replaced with a small random background. This step is necessary to prevent to edge of the camera cold stop from being interpreted as part of the source image. Figure 16 contains the same treatment applied to g(x,y).

Figure 16. The Generated Image g(x,y) and its Fourier Transform

46

The leftmost image in figure 16 contains the geometrically predicted image of the source in figure 15 and the rightmost image contains its Fourier transform.
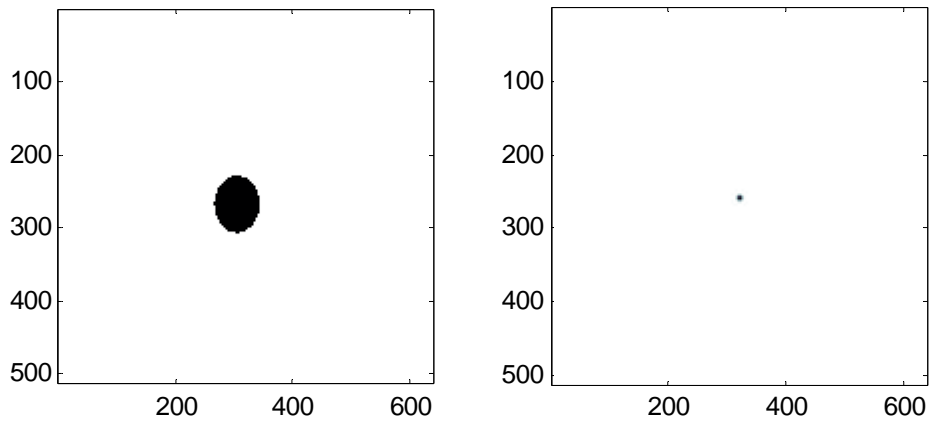
The two image functions and their Fourier transforms provide sufficient evidence of proper sampling. Both transformed functions are nonzero over only a finite region in Fourier space. Functions that exhibit this behavior (or closely approximate it) are considered to be bandlimited. Functions of this class enjoy a special property: a properly sampled bandlimited function can be used to completely reconstruct the original analog function (Goodman,1996: 23). In general, Fourier transforms are periodic. Bandlimited functions are properly sampled when this periodic structure does not overlap (a phenomenon known as aliasing). It is clear from figures 15 and 16 that no such overlap occurs. Consequently, both functions are adequately sampled.

Iterating the RL Algorithm.

The Richardson-Lucy algorithm does not come packaged with a definitive method for determining the number of required iterations. Qualitatively, this cutoff should occur once subsequent iterations no longer improve significantly on the previous approximation. To quantify this concept, the sum of the squared error between neighboring approximations, E_{sq}, is introduced

$$E_{sq} = \sum_x \sum_y \left[h_k(x,y) - h_{k+1}(x,y) \right]^2 \tag{5.5}$$

Unless E_{sq} goes to zero, the cutoff iteration is left to some interpretation. Figure 17 contains a semilog plot of E_{sq} versus iteration number. This particular data comes from the application of the Richardson-Lucy algorithm on the $g(x,y)$ and $f(x,y)$ combination provided in the previous discussion.

47
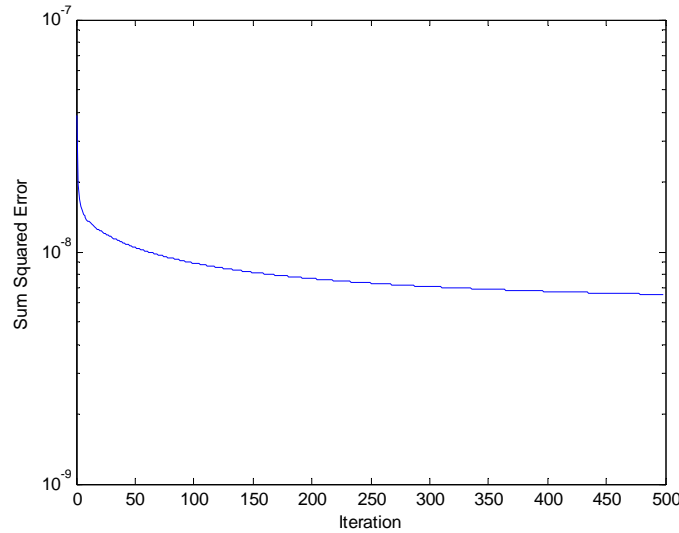
Figure 17. Sum Squared Error of the Richardson-Lucy Algorithm

The magnitude of the squared error, large or small, is of little practical use (recall the

h(x,y) is normalized and is therefore unitless). Instead, the cutoff iteration is selected

based on the (somewhat subjective) determination of where slope of the E_{sq} curve is

effectively zero. At 500 iterations, the E_{sq} curve presented above appears to meet this

criterion.

The Estimated Point Spread Function.

Figure 18 contains the image of the PSF, $h_{500}(x,y)$, corresponding to the work laid

out in the previous discussion.

Figure 18. The Richarchson-Lucy Estimated PSF

Recall that this is an estimation of the PSF at around 4.3 um. The next step is to create a generalized phase screen out of this information that can be used to describe point spread functions at all wavelengths.
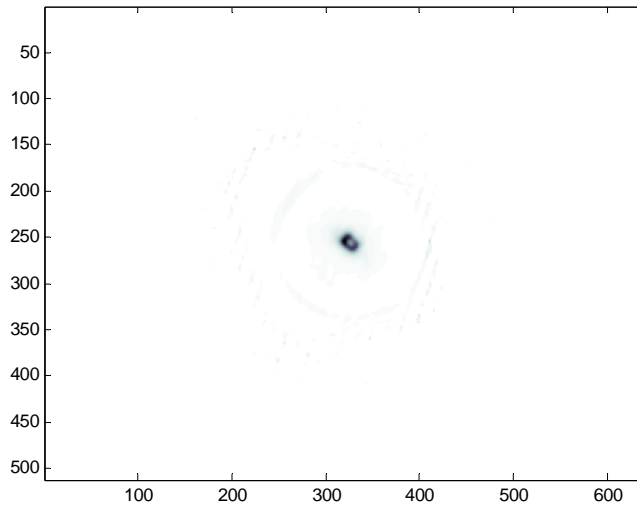
The Gerchberg-Saxton Phase Retrieval Algorithm

The Gerchberg-Saxton Phase Retrieval Algorithm (Gerchberg, 1971:237) estimates diffraction plane phase given measurements of the intensity in the diffraction and imaging planes. For this specific application, the point spread function generated by the Richardson-Lucy algorithm provides the intensity pattern in the imaging plane and the intensity in the diffraction plane is estimated to be constant with respect to position. As a result, the sampling scheme used to implement the Richardson-Lucy algorithm is maintained.

According to the author, the GS algorithm, presented schematically in figure 19, takes advantage of the fact that a change in amplitude in one plane (diffraction or image)

is the result of a change in both phase and amplitude in the other. Gerchberg goes on to show that the squared error between the image reconstructed using the phase from his algorithm, $h_k(x,y)$, and the original image (in this case, the Richardson-Lucy recovered PSF), $h_{rl}(x,y)$, must decrease or remain constant with each successive iteration.

$$\sum_x \sum_y \left[h_{rl}(x,y) - h_{k+1}(x,y) \right]^2 <= \sum_x \sum_y \left[h_{rl}(x,y) - h_k(x,y) \right]^2 \tag{5.6}$$

Note that the subscript k has been recycled to again refer to iteration index.
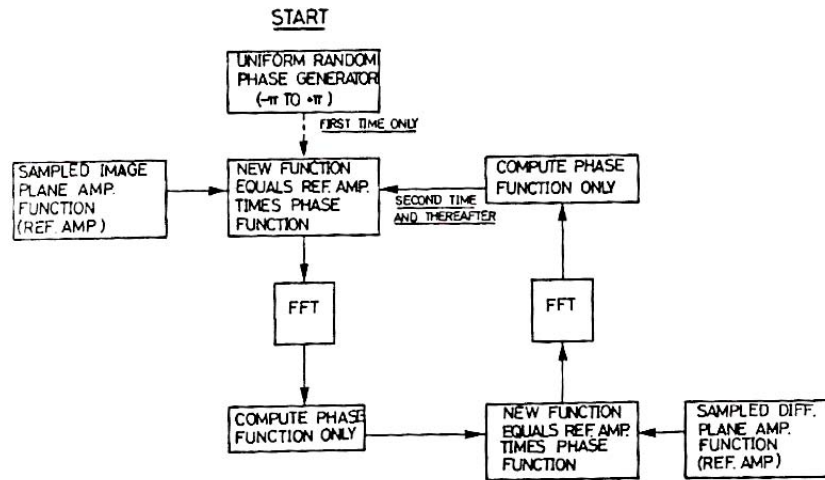
Figure 19. Schematic Representation of the Gerchberg-Saxton Algorithm (Gerchberg, 1972:239)

Iterating the Gerchberg-Saxton Algorithm.

Equation (5.6) leaves open the possibility that the algorithm will stagnate before perfect reconstruction of the point spread function is achieved (i.e. when the squared error is driven to zero). Figure 20, a plot of this squared error over 500 iterations, shows that the Gerchberg-Saxon reconstruction of the PSF $h_{rl}(x,y)$ is, in fact, subject to this predicted stagnation.

50
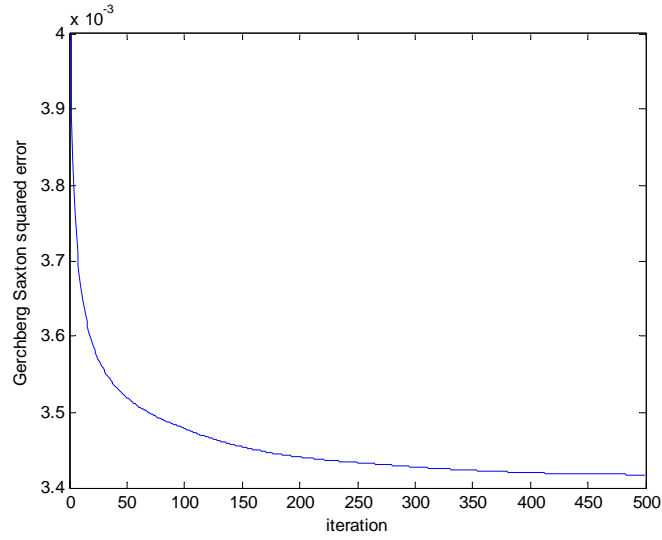
Figure 20. Stagnation of the Gerchberg-Saxton Phase Retrieval Algorithm

Comparing Recovered Point Spread Functions

Ultimately, the impact of this imperfect reconstruction is difficult to assess out of the context of the finished product but, in the interval, a comparison between the GS estimated PSF and the RL recovered PSF will suffice.

Figure 21 contains the Richardson-Lucy recovered point spread function from figure 18, enlarged and cropped so that a direct comparison can be made between it and the Gerchberg-Saxton estimated point spread function.

51
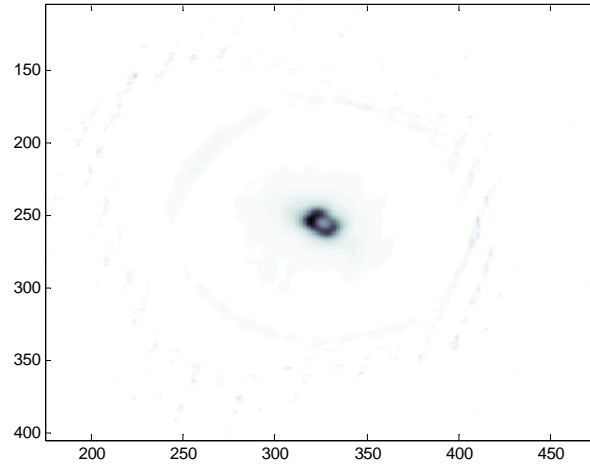
Figure 21. Enlarged Richardson-Lucy Point Spread Function

For comparison, figure 22 contains the Gerchberg-Saxton estimation of the point spread

function in figure 21.
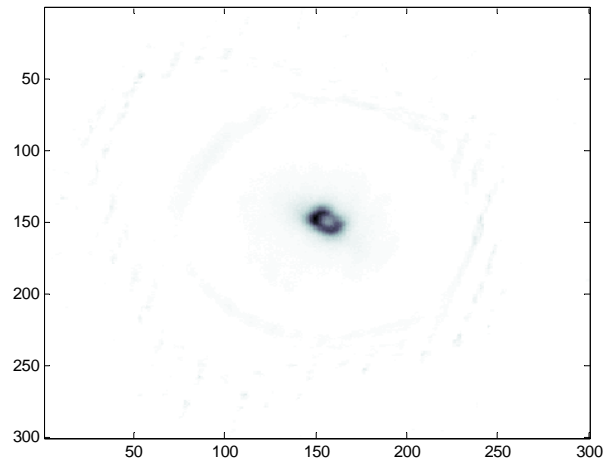
Figure 22. PSF Generated from Gerchberg-Saxton Recovered Phase

Visual inspection seems to indicate a strong resemblance between the two figures

but the two are clearly not identical. Notably, more power appears to be concentrated at

the center of the image in figure 21 and, by comparison, the central feature in figure 22 is

more amorphous. Predictably, this center broadening will manifest itself in the CT model as a more dispersed source though, as stated previously, the total impact of this problem is best left for the final analysis.

Reiteration the entire process places the calculation of the phase screen in its proper context. The recovered phase, γ_{prop}, is scaled to the appropriate wavelength and combined with the phase generated by the prism model to produce a model of the point spread function on the focal plane array. The mechanism for this process was established in chapter IV. The geometric image of the source is convolved with the point spread function to produce a monochromatic image of the source. Many such images are then combined to produce a complete simulation of the CT response to the source input. At this point the model is complete and attention can turn to the process of comparing simulated images with imagery made in the laboratory.

VI. Measurements and Mechanisms for Comparing Results

The model defined in chapters IV and V, though in general quite flexible, places certain requirements on how laboratory measurements must be prepared and processed. These requirements fall into five categories: nonuniformity correction, background suppression, image alignment errors, prism alignment errors, and rotation errors. With the exception of responsivity, each of the other requirements are dealt with as individual parameters. Before exploring these parameters, a sufficient explanation of the statistics of an image captured from the CT is in order.

Techniques such as correlation and sum squared error provide a means for determining which simulation parameters best fit a particular result. Both of these mechanisms will be applied in this analysis but neither can be described as a definitive test for measuring the overall effectiveness of the simulation. An excellent example of this dilemma can be made by reaching ahead into chapter VII and examining some correlation results. Two simulations are made and correlated with a measurement resulting in correlation coefficients of 0.9133 and 0.9895. Both correlations turn out to be close to 1 (1 being complete correlation) but one of the simulated images has been rotated by 90° from the image it was intended to simulate. The two results appear favorable because the intensity pattern changes in the center of the image but most of the pixels considered are not affected by the rotation and hence remain highly correlated. This comparison clearly shows that the 90° rotated simulation is not the better of the two choices though the result provides no insight into overall agreement with the collected data.

Image Statistics

Model and data agreement is best couched in terms of the noise statistics of the image. The values recorded at each pixel are a quantized representation of the number of incident photons being absorbed in the pixel's volume over some interval. The probability of the camera's electronics reporting any particular value is governed by either photon, quantization, or electronic noise depending on the intensity of the source and the quality of the instrument. Once this distribution is identified, the quality of the simulated data can be expressed, pixel by pixel, in terms of the probability of making a measurement that exactly matches the simulation. The outward form of this expression is represented by the number of standard deviations a simulated pixel is away from its measured counterpart.

The Poisson Distribution.

According to E. L. Dereniak, the optical system described above should follow Poisson statistics:

> ...photons follow Poisson statistics for all practical detector applications. That is, for visible and near infrared applications, low temperature blackbodies, and short wavelength [radiation] (hv >> kT), the photon noise follows Poisson statistics (Dereniak, 1996: 156)

As a result, the Poisson distribution is used as a theoretical model for the CT camera image statistics. For the intended purpose, the most important characteristic of this distribution relates the mean, μ, to the standard deviation, σ.

(Kreyszig, 1999:1081)

$$\mu = \sigma^2 \qquad\qquad (5.7)$$

To determine the applicability of this distribution, the CT optical system was configured to take 700 frames (the maximum number allowed by the camera buffer) of a temporally constant blackbody source. The mean and standard deviation of these images is measured and compared to a theoretical Poisson distribution. Figure 23 contains a cross section of the focal plane array though the center of the source image along with the theoretical and measured error bars.
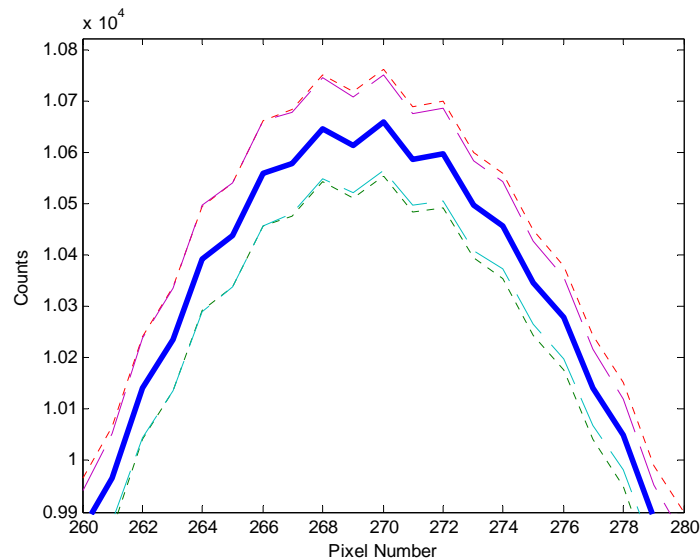
Figure 23. Image Cross Section with Theoretical and Measured Error Bars

The thick solid line in figure 23 is the mean value of each pixel, enumerated along the x axis and the error bars are identified by the dashed lines. Short dashes identify the theoretical Poisson error bars and long dashes identify the actual error bars. The error bar overlap is not perfect, but given the sample size (700 frames) the difference is justifiable.

Sufficient evidence of a Poisson distributed system exists between the combination of the collected noise data presented in figure 23 and Dereniak's assertions for regions where signal is present. Though not included in the plot, regions of the focal

plane where little or no signal was detected did not follow Poisson statistics. This result is not surprising because other forms of noise become more prevalent in the absence of signal (i.e. dark current). Failure of the statistical model in these regions is acceptable because they have little impact on the model verification process.

Processing Images

The noise statistics of an image are presented first so that the effects of the image processing procedure can be better understood. As stated previously, the model presented in this research requires that measurements be made and processed in a certain way. The remainder of this section will deal with this processing method and, where appropriate, its effects on the statistical fit of the model.

Nonuniformity Correction.

Pixel response is a combination of pixel responsivity and the connected amplification electronics. Nonuniformity correction (NUC) is applied to all imaging systems with more than one detector element to compensate for variations in individual pixel bias and gain. This process, also referred to as flat field calibration, is carried out by exposing the entire focal plane array to sources of uniform intensity and adjusting the gain and bias of each pixel so that their response is equivalent at these of these points. Figure 24 is a graphical depiction of this process.
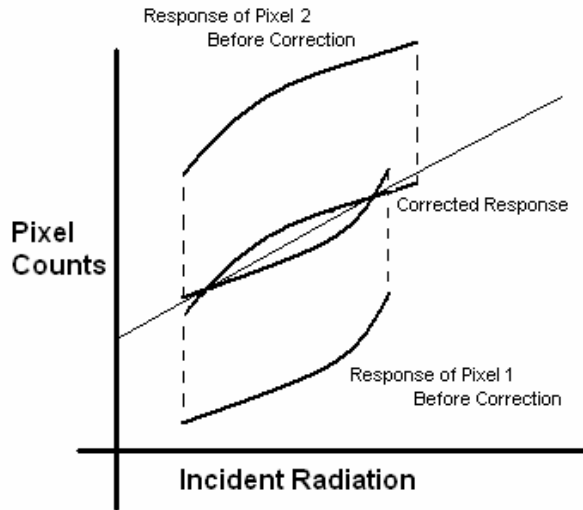
Figure 24. Two Pixel Nonuniformity Correction

As shown in the graphic, the NUC is carried out by matching the count output of

two pixels at two known levels of irradiance. Nonuniformity correction is applied in the

CT system by replacing the focusing lens with a uniform blackbody source and making

measurements at two known temperatures. The details of NUC processing are carried out

by software provide by the camera's manufacturer. The NUC is sensitive to thermal

cycling therefore a new correction is made each time the camera is cooled from room to

liquid nitrogen temperature.

Background Suppression.

The model makes no allowance for photons generated from anywhere besides the

intended target whereas, in the laboratory, it is impossible to isolate the intended target in

a single measurement. This background may include thermal photons generated inside of

the CT system, photons scattered onto the FPA from outside the system, and photons

58

from the scene surrounding the target. Eliminating or suppressing these background sources is dealt with though a combination of physical and software means.

The effects of photons generated inside of the CT system can be subtracted away from the target image assuming this background remains constant and can be isolated from the scene. The internal background is made constant by shrouding the system with black velvet cloth. As an additional precaution, the distance between the focusing lens and the camera face is enveloped by a cardboard tube. Furthermore, the region in front of the leading aperture is enclosed with thick packaging material to eliminate reflections from the laboratory floor. These devices emit weakly over the bandpass but the effective internal background is limited to only to this emission. Figure 25 is a picture of the shrouded CT system.

Figure 25. The Shrouded CT System

Having isolated the sensor from its surroundings, the next step is to isolate the background from the blackbody source. This is accomplished taking an image of the scene (with the source target covered) seconds before the target image is made. The background image contains the internally and externally generated background but not

59

the source or its immediate surroundings (the blackbody and the face of the apparatus that contains it). To emphasize the importance of this step, figure 26 contains a slice of an image made before background subtraction (left) and the same slice of an image after background subtraction (right).
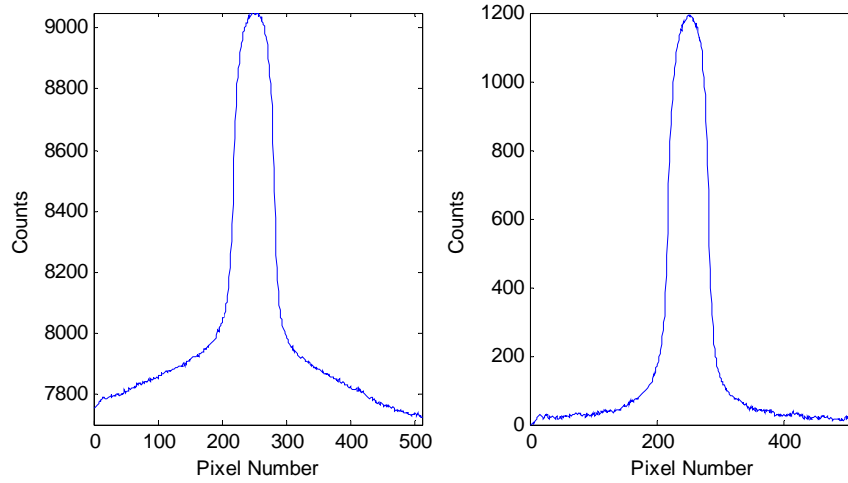

Figure 26. Images Before and After Background Subtraction

As seen in figure 26, a small bias remains after background subtraction. This remaining background is likely the result of thermal emission from the region immediately surrounding the blackbody cavity that, during collection of the background image, is obscured along with the cavity. Suppression of this effect is treated as an adjustable parameter whose selection is based upon the image correlation coefficient.

$$C = \frac{\sum_{i=1}^{n}\sum_{j=1}^{n}M(i,j)N(i,j)}{\sqrt{\sum_{i=1}^{n}\sum_{j=1}^{n}M(i,j)^2 \sum_{i=1}^{n}\sum_{j=1}^{n}N(i,j)^2}} \quad (5.8)$$

where M and N represent the measured and simulated images. The value of the suppression parameter is selected based upon its ability to maximize the C. The

60

correlation coefficient is more appropriate for selection of this parameter than squared error because squared error emphasizes intensity differences where magnitudes are large while the correlation coefficient weighs the contribution of each pixel equally. This residual background represents a small percentage of the signal peak, but its effect on the model and measurement comparison in regions where the signal is small can not be understated. Subtraction of this constant background gives rise to small regions where the resulting intensity is negative. This unfortunate effect is mitigated by setting all negative values to zero.

Registration Errors.

Despite efforts to precisely align the source image with the center of the focal plane, some discrepancy will inevitably exist. To correct this problem, a simple image registration algorithm is applied to the model image. The algorithm shifts the model image by one pixel in each of 8 separate directions and compares the result to the measured image using the squared error technique. The shift that provides the least squared error becomes the new center of the model image and the process repeats itself until the central pixel provides the least squared error.

There are two potential drawbacks to this algorithm. First, registration is limited the precision provided by shifts made in whole pixel increments. Second, the algorithm has no mechanism for determining whether the squared error minimum is local or global in nature. The first issue can be reduced by selecting a more sophisticated algorithm if greater precision is necessary though the results will show that, at least for this incarnation of the model, this is not the case. The second issue is protected against by

visual inspection of the results (a significant misalignment of the images is readily apparent).

Prism Alignment and Rotation Errors.

Mathematically, prism alignment errors are expressed in terms of the angle φ in equation (3.10) and the surrounding discussion. φ is treated as model parameter that is minimized simultaneously with the rotation error angle using the correlation method described above. Minimization of this parameter may also suffer from the problem of stumbling into local minima but, as care is taken to properly align the prisms, alignment errors of this type are small.

Prism Rotation angle errors are also eliminated parametrically. As stated previously, the circular symmetry of the source allows for rotation of the composite image. After an initial approximation of the rotation angle is made in the model, small corrections are applied though an additional application of the rotation routine discussed in the previous chapter. Like alignment error minimization, rotation error minimization is accomplished though the application of the correlation technique.

VII. Results, Analysis, and Conclusions

The measurement techniques and model registration processes outlined in chapter VI are applied here to four broadband (3-5 um) CT images. The measured images represent a 400°C blackbody with a manufacturer specified emissivity of 0.97 or greater (EOI, 2004: 1). Measurements were made sequentially over an approximate 30 minute period with identical camera settings (frame rate, integration time, etcetera) and laboratory atmospheric conditions. All other conditions being equal, the difference between each image lies in a change of rotation angle (90° each time) of the prism assembly. Each measurement is presented along with a corresponding simulated image, a model fit map, and a brief explanation of the parameters selected to make the fit.

The model fit map contains a pixel by pixel representation of the agreement between the simulation and the model. The value reported for each pixel expresses the probability of a match in terms of the number of Poisson standard deviations that the model value lies away from the measured value.

Results

Comparison 1: 275° Rotation Angle.

Figures 27, 28, and 29 contain (in order) the CT measurement, the simulation, and the fit map. The best fit was arrived at using a background bias of 320 counts (2.2% of the peak) and a prism alignment error angle of 0.1° (the rotation angle was also fit parametrically). Registration required a net shift of 2 pixels. Overall correlation between the two images is 0.9891.
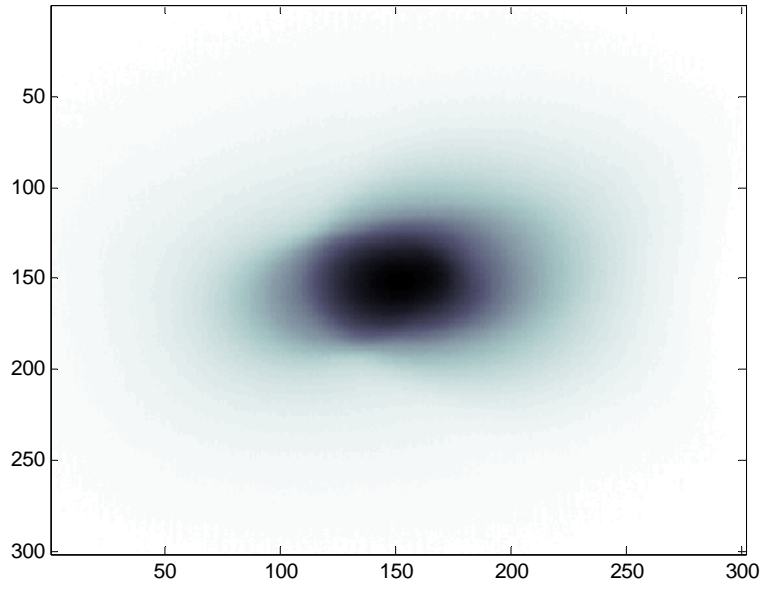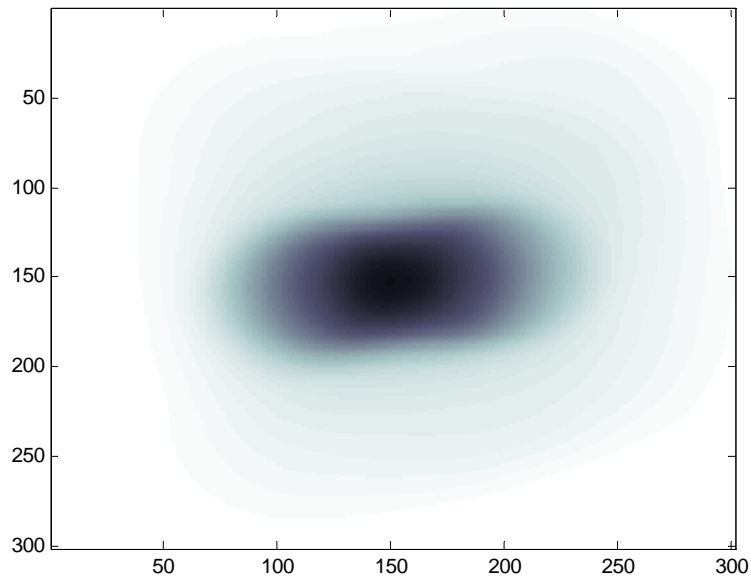
Figure 27. 275° Prism Rotation Angle Data

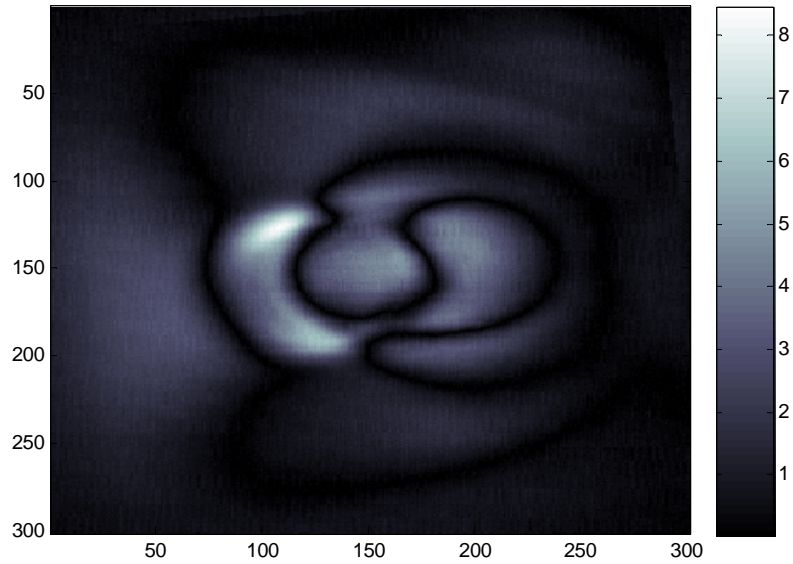Figure 28. 275° Prism Rotation Angle Simulation

Figure 29. 275° Prism Rotation Angle Fit Map

The peak error shown in figure 29 is 8.53 standard deviations and the average error in the region specifically containing the signal is 1.87 standard deviations.

Comparison 2: 184.5° Rotation Angle.

Figures 30, 31, and 32 contain the CT measurement, the simulation, and the fit map of the second set of measurements. The best fit was arrived at using a background bias of 390 counts (3.02% of the peak) and a prism alignment error angle of 0°. Registration required a net shift of 6 pixels. Overall correlation between the two images is 0.9894.
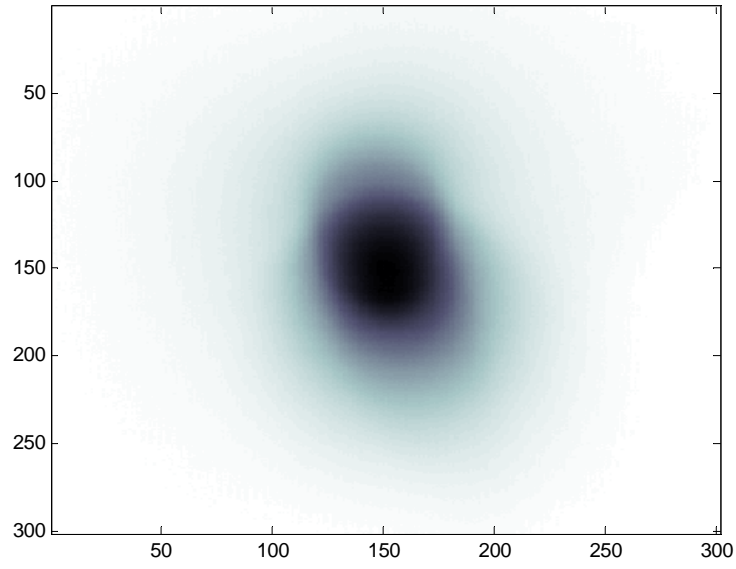
Figure 30. 184.5° Prism Rotation Angle Data

Figure 31. 184.5° Prism Rotation Angle Model

66

Figure 32. 184.5° Prism Rotation Angle Fit Map

The peak error shown in figure 32 is 7.15 standard deviations and the average error in the region specifically containing the signal is 1.35 standard deviations.

Comparison 3: 100° Rotation Angle.

Figures 33, 34, and 35 contain the CT measurement, the simulation, and the fit map of the third set of measurements. The best fit was arrived at using a background bias of 380 counts (3.00% of the peak) and a prism alignment error angle of 0.1°. Registration required a net shift of 13 pixels. Overall correlation between the two images is 0.9895.
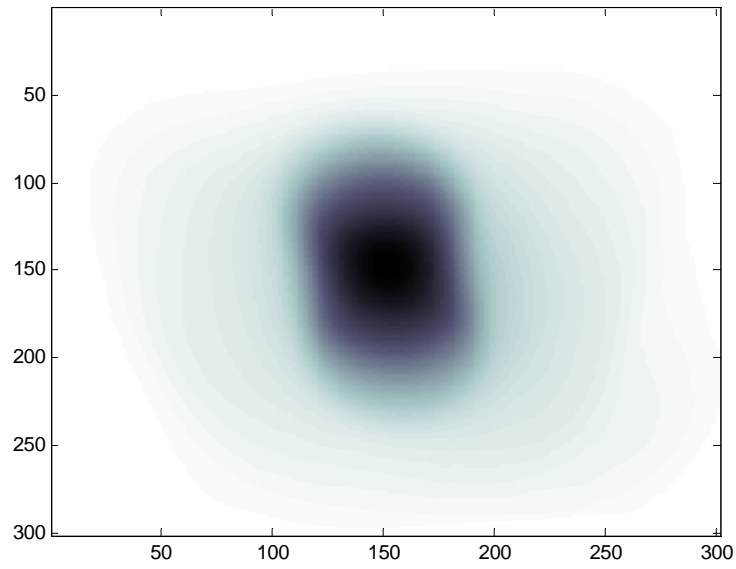
67

Figure 33. 100° Prism Rotation Angle Data
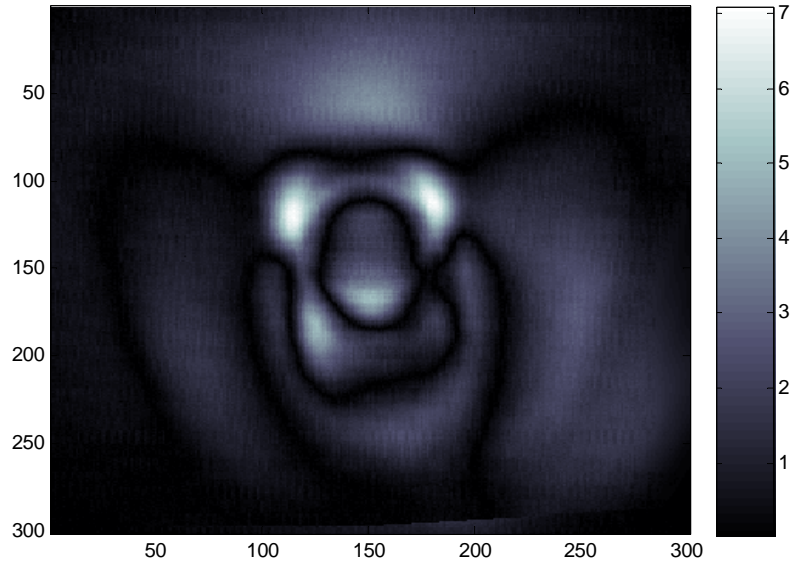

Figure 34. 100° Prism Rotation Angle Simulation

68

Figure 35. 100° Prism Rotation Angle Fit Map

The peak error shown in figure 35 is 7.11 standard deviations and the average error in the region specifically containing the signal is 1.65 standard deviations.

Comparison 4: 14.5° Rotation Angle.

Figures 36, 37, and 38 contain the CT measurement, the simulation, and the fit map of the fourth set of measurements. The best fit was arrived at using a background bias of 340 counts (2.44% of the peak) and a prism alignment error angle of 0.2°. Registration required a net shift of 3 pixels. Overall correlation between the two images is 0.9901.
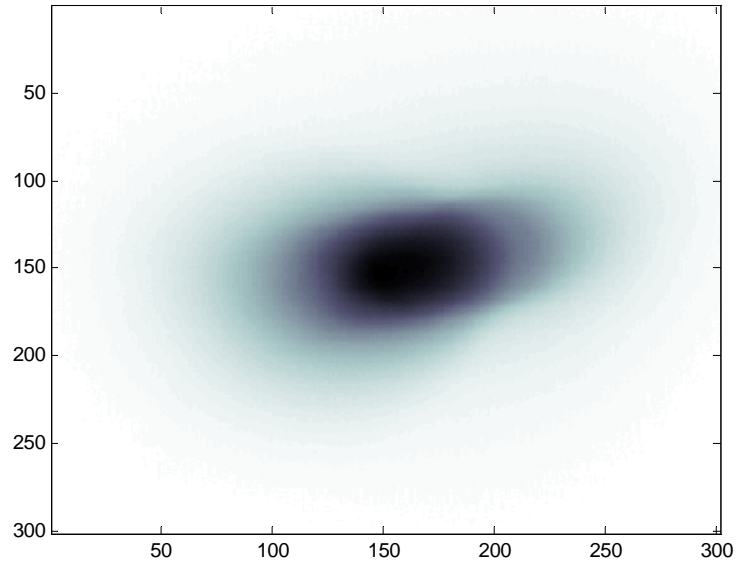
69
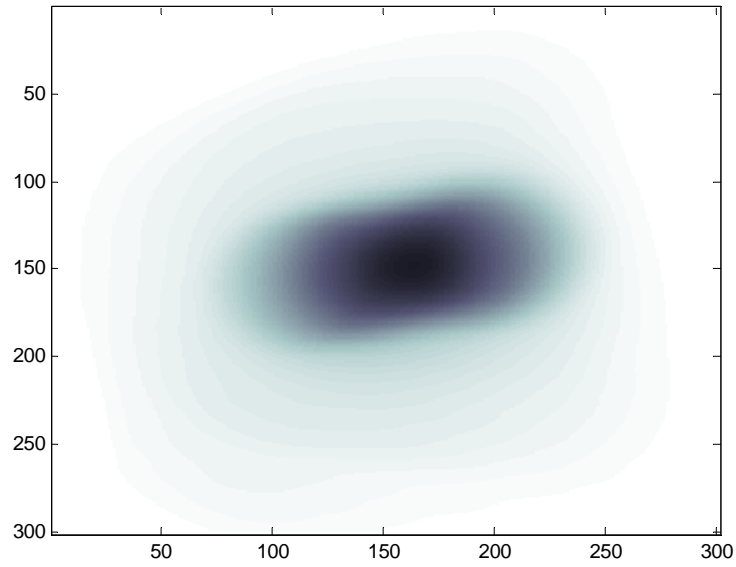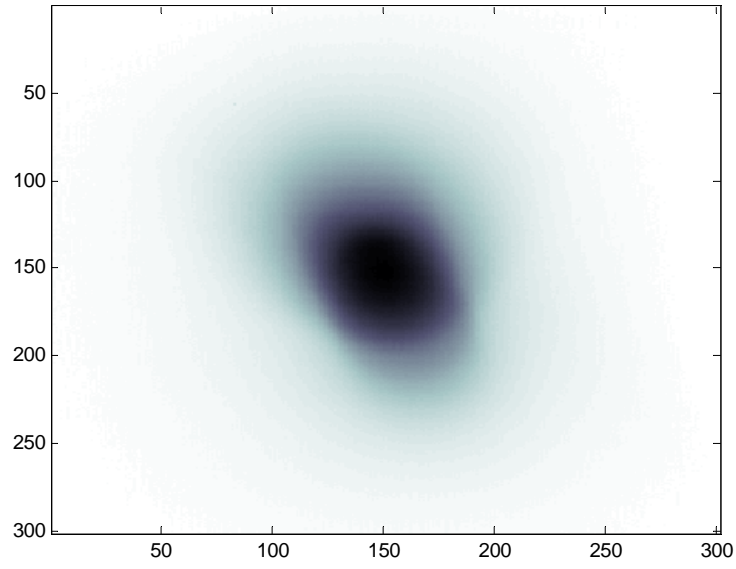
Figure 36. 14.5° Prism Rotation Angle Data

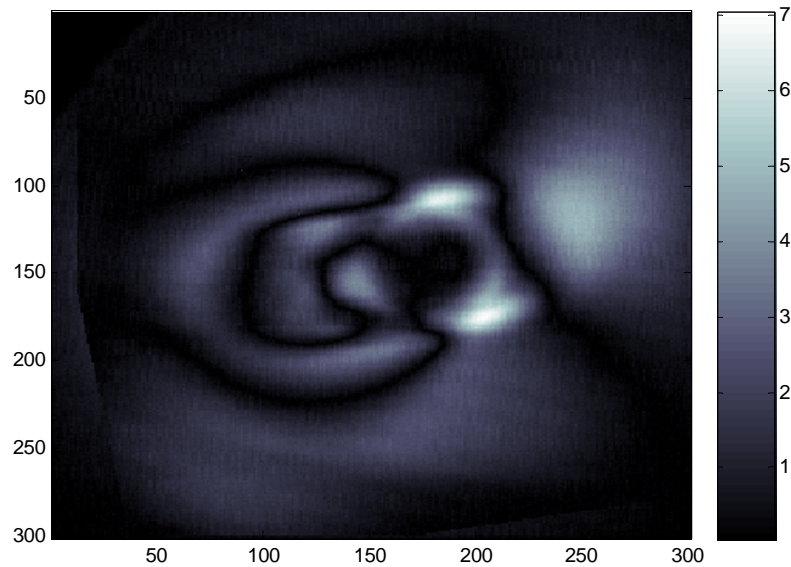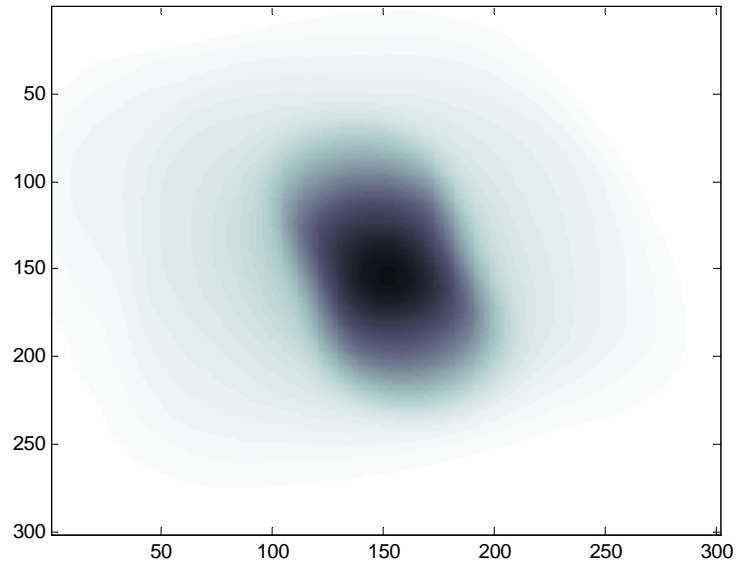Figure 37. 14.5° Prism Rotation Angle Simulation
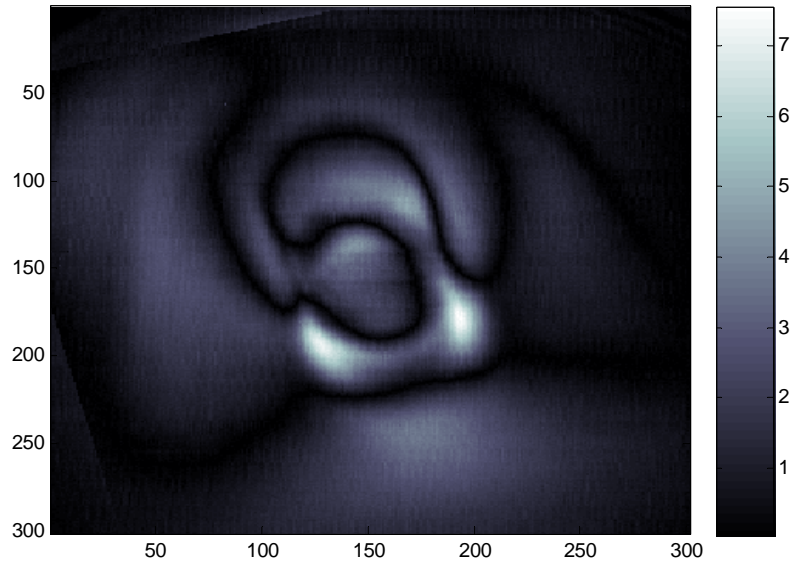
Figure 38. 14.5° Prism Rotation Angle Fit Map

The peak error shown in figure 38 is 7.62 standard deviations and the average error in the

region specifically containing the signal is 1.76 standard deviations.

Summary of the Experimental Data.

Table 3 contains a consolidated version of the information supplied above to

facilitate the discussion in the following sections.

Table 3. Results from Four Comparisons

Comparison	Bias (counts)	Rotation Angle (deg)	Alignment Error (deg)	Correlation Coefficient	Max Error (std dev)	Mean Error (std dev)
1	320	275.0	0.1	0.9891	8.53	1.87
2	390	184.5	0.0	0.9894	7.15	1.35
3	380	100.0	0.1	0.9895	7.11	1.65
4	340	14.5	0.2	0.9901	7.62	1.76

71

Analysis

With the exception of rotation angle, the comparison results are similar for each of the four data sets. The following section describes how each of the columns in table 3 can be used to reinforce or detract from this opinion. Conclusions based on this analysis are presented in the following section.

The background bias floats between 320 and 390 counts or 2.20% to 3.02% of the signal peak. The relative size and consistency in background bias helps to reaffirm the initial justification for including this parameter, which was to minimize the impact of emission from the area immediately surrounding the blackbody cavity. Recalling that the standard deviation of the Poisson distribution goes with square root of the measured value, an extra 300 counts could have easily been interpreted as additional error in places where no such error existed.

Surprisingly, the only apparent major discrepancy in the experiment comes from rotation angle. Following the order in which the measurements are presented, each subsequent measurement should represent a net rotation of $90°$. Rotation between the first two measurements is almost exactly that but the angular difference between the second and third measurements is $85.5°$. Confounding matters further, the difference between the third and fourth measurements is $114.5°$. This discrepancy is apparently a motor control issue and, since the model can compensate for any rotation angle, its impact on this research is negligible.

Prism alignment error, the apparent angular difference between the theoretical orientation of each prism and the actual orientation, varies slightly across the four

72

measurements (0 to 0.2 degrees). Since no adjustments were made to the prism assembly in the interval between measurements, two possible explanations for this shift exist. First, a physical shift may occur during prism rotation though this seems unlikely as both prisms are held in place via set screws. Second, the shift represents numerical error in the model and measurement reconciliation software. Given that the relative error is small and that it appears to follow no particular pattern, the second explanation would appear to be the most plausible.

Though all four correlations are quite high, the correlation between the measured and simulated images do not speak to the overall merit of the simulation based upon magnitude alone (anecdotal evidence of this statement is provided in the example given in the previous chapter). Rather, the correlation's relevance to this research is derived from its consistency across the four measurements. Note from table 3 that the maximum difference between any two correlations is limited to 0.001. By itself, this piece of information is an indication of consistency in the results, but not necessarily an indication of accuracy.

Two important points come out of the measurement of maximum error across the four sets of results.   First, the max error is spread out between 7.11 and 8.53 standard deviations, which is another indication of consistency throughout the results. Second, the max error is always found in the same regions of dispersion as seen in figures 29, 31, 34, and 37. In other words, the maximum error regions (represented by two bright lobes in the figures) correspond to regions of the focal plane affected by dispersion in the same spectral region.

This error may be the result of a variation in focal length of the three lens system as a function of wavelength. This variation will manifest itself physically as a gradient in magnification. A return to geometric optics helps to test this hypothesis. Focal length, f, is determined for thin lenses in air using the lens maker's equation (Hecht, 2002:158)

$$\frac{1}{f} = (n_l - 1)\left(\frac{1}{R_1} - \frac{1}{R_2} \right) \tag{7.1}$$

where R_x represents the curvature of the lens and n_l is the refractive index of the lens. The in focus magnification from equation (3.28) is approximated as a function of wavelength under the assumption that the manufacturer's specified focal length occurs at 4 um (the center of the CT bandpass). Figure 39 is a plot of approximate magnification as a function of wavelength.
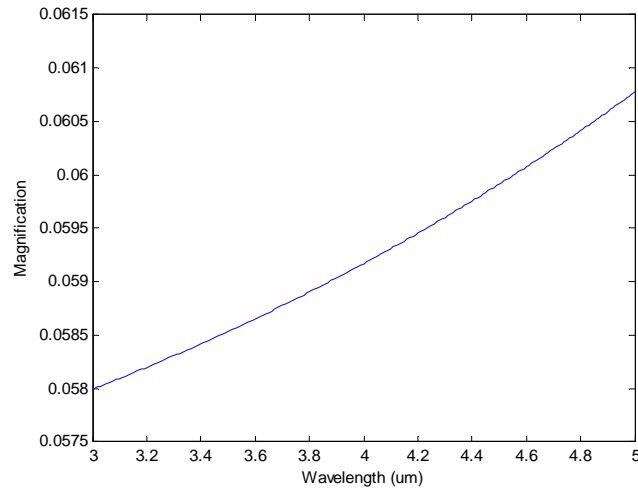

Figure 39. Magnification as a Function of Wavelength

The overall change in magnification is subtle but certainly enough to affect the outcome of the simulation. Note that figure 39 approximates the *in focus* magnification over the bandpass; in reality, the sensor can only be truly in focus at one wavelength.

74

Consequently, figure 39 is useful for demonstrating that the effect exists, but provides nothing practical to add to the simulation.

Alternatively, the apparent change in magnification may be the result of distortion, which is defined to be a variation in transverse magnification with respect to off axis image position (Hecht, 2002: 266). Though it can't be ruled out, the distortion argument is more difficult to justify because the regions of greatest error appear to correspond with a change in spectral rather than spatial positioning.

Mean error is also consistent throughout the series of comparisons. This figure of merit is bracketed between 1.35 and 1.87 standard deviations, though this range may be somewhat artificially depressed. Inspection of each fit map shows apparent curves of near zero error that wind throughout the scene. Though the pixels values of the simulation and measurements are nearly equal in these regions, this is probably due to coincidental overlaps in the two intensity patterns rather than the manifestations of an exact model. Figure 38 helps to illustrate this concept.
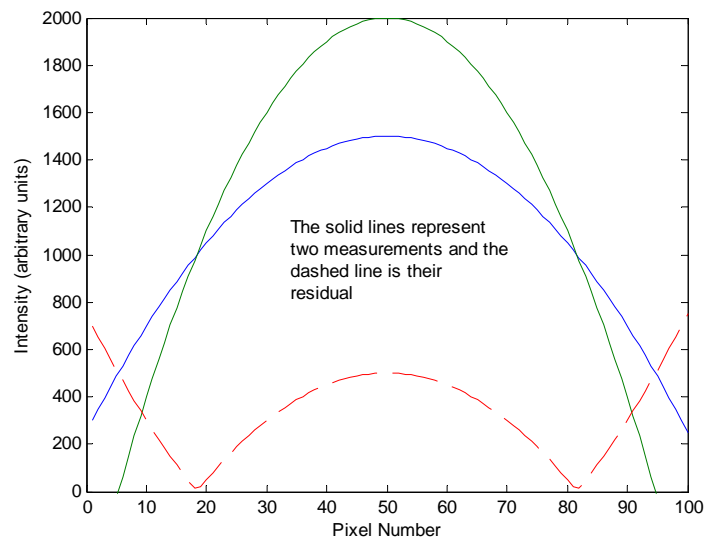

Figure 40. Example of Intensity Pattern Overlap

The two imaginary intensity profiles in figure 38 overlap in two locations. This overlap creates regions where the residual is numerically small even though the overall fit is no better in these regions than in anywhere else. This effect, extrapolated into three dimensions, is readily apparent in all four of the fit maps and is responsible for lowering the average error though its overall impact is difficult to assess.

Conclusions

Research Summary.

The purpose of this research was to demonstrate the validity of a phase screen modeling approach by simulating a chromotomographic hyperspectral imaging system. The progression of this document mirrors the chronological progression of the research: constructing the CT sensor (chapters II and III), modeling the sensor (chapters IV and V), and making measurements for comparison (chapters VI and VII). Ultimately, success or failure of the model was based on a measure of its statistical agreement with the measured data.

Assumptions.

Three primary assumptions were built into the modeling process. The first (and predominant) assumption was that the CT system is linear and invariant in intensity over the region of the focal plane occupied by the image. This assumption is critical if the Fourier transform model of propagation is valid. Second, radiation entering the focusing lens can be modeled as a corruption of a collimated beam. This assumption, which primarily ignores the effects of diffraction during the collimation process, paved the way for the single lens approximation. Third, all aberrations, whether they be from alignment of or innate to the optical system or its components, can be captured and reproduced in

76

the phase screen measurements. In one sense, this assumption is a restatement of the first but it extends the definition to include radiation of all wavelengths.

In addition to the primary assumptions, which are unavoidable, several secondary assumptions crept into the research. These assumptions include:

(1) Any deviation from perfect prism alignment is described in the model.
(2) The blackbody source is uniform and Lambertian.
(3) All photons entering the leading aperture of the sensor are accounted for.
(4) Reflected radiation can be ignored

Conclusions.

This research has shown that, over some field of view and some spectral range, the phase screens generated using the phase retrieval process can be used to approximate the intensity patterns produced by the chromotomographic imaging system. The overall agreement between the measured and simulated data (expressed in terms of the generally low mean error) is evidence of this statement.

Regions where the simulated and measured data disagree most appear to be dominated by either an off-axis magnification effect (distortion), or a chromatic variation in magnification. These potential sources of error can be reduced or eliminated by adjusting the sensor (achromatic lenses, shifting or reducing the field stop) or by generating multiple phase screens at regular intervals to compensate for these effects.

The successful assimilation of the phase screen technique into the Fourier propagation model provides a conceptual basis for applying the same technique to a modified CT image reconstruction algorithm.

Recommendations for Future Research.

The conclusions statement, statement of assumptions, and original motivation for this research all lend themselves immediately to a list of future research projects. If the phase screens are to be imported into a chromotomographic deconvolution algorithm, then the next appropriate research step is to identify the largest field of view over which the primary assumptions apply. Concurrent efforts should be spent identifying the useful spectral bandwidth of any particular phase screen.

Recall that the Gerchberg-Saxton phase retrieval algorithm could not generate a phase screen that perfectly reproduces the Richardson-Lucy point spread function. While the utility of Gerchberg-Saxton is well known, other algorithms exist that can perform the same function (Schulz, 1992: 1266). Future research should concentrate on selecting another phase retrieval algorithm or modifying an existing one to suit the specific needs of the CT optical system.

Modeling research could continue by expanding the single propagation model into a multi-propagation model. This step would increase the complexity of the phase retrieval process immensely by requiring that a separate phase screen be provided for each element in the optical system. Since the phase screen conveys both innate and alignment aberrations, each screen after the focusing lens would have to be determined by some sort of deductive process. If successful, this research step would effectively eliminate the second primary assumption.

Bibliography

Berk A. and others. *MODTRAN4 Version 3 Revision 1 User's Manual*
    Air Force Research Laboratory / Space Vehicles Directorate, Hanscom AFB, MA
    11 Feb 2003

CTHIS Sensor Products, Solid State Scientific Corporation CT products website.
    1 September 2004 http://www.solidstatescientific.com/prods/cthis/index.php

Dearinger, Anthony J. *Simulating a Chromotomographc Sensor for Hyperspectral
    Imaging in the Infrared.* MS thesis, AFIT/GE/ENG/04-05. School of
    Engineering and Management, Air Force Institute of Technology (AU), Wright
    Patterson AFB OH, March 2004 (ADA)

Dereniak, Eustace L. and G.D. Boreman. *Infrared Detectors and Systems*
    New York: John Wiley and Sons, 1996

EOI Home Page, Electro Optical Industries cavity blackbody products. 13 October 2004
    http://www.electro-optical.com/index2.htm

Gerchberg, R.W. and W.O Saxton. "A Practical Algorithm for the Determination of
    Phase from Image and Diffraction Plane Pictures" *Optik* Vol 35 (No. 2): 237-246
    (1972)

Goodman, Joseph W. *Introduction to Fourier Optics* (2nd Edition)
    Boston: McGraw-Hill, 1996

Gustke, Kevin. *Reconstruction Algorithm Characterization and Performance Monitoring
    in Limited-Angle Chromotomography.* MS thesis, AFIT/GE/ENG/04-05.
    School of Engineering and Management, Air Force Institute of Technology (AU),
    Wright Patterson AFB OH, March 2004 (ADA)

Hecht, Eugene. *Optics* (4th Edition) San Francisco: Addison Wesley, 2002

ITRES – Image Gallery: Agriculture (Hyperspectral Data Cube), ITRES corporate
    website. 7 September 2004 http://www.itres.com/docs/agri1.html

Kreyszig, Erwin. *Advanced Engineering Mathematics* (8th Edition) New York: John
    Wiley and Sons

Lanteri, Henri and others. "Blind Deconvolution using the Richardson-Lucy Algorithm."
    Proceedings of the SPIE Vol 2312: 182-192 (December, 1994)

Mooney, Jonathan M. "Angularly Multiplexed Spectral Imager." *Proceedings of SPIE* Vol: 2480: 65-77 (June, 1995)

Mooney, Jonathan M. "High-throughput hyperspectral infrared camera," *Journal of the Optical Society of America A:* 2951-2961 (November, 1997).

Murguia, James E. "A Compact Visible/Near Infrared Hyperspectral Imager," *Proceedings of SPIE* Vol 4028: 457-468 (July, 2000).

Orson, Jay A. and others. "Infrared Signatures from Bomb Detonations," *Infrared Physics and Technology* Vol 44: 101-107 (2003)

Pedrotti, Frank L. and Leno S. Pedrotti. *Introduction to Optics* (2nd Edition), Upper Saddle River: Prentice Hall Inc, 1987

Roggemann, Michael C. *Imaging Through Turbulence*, Boca Raton: CRC Press, 1996

SBFB Camera User's Guide (author unknown), Santa Barbara Focalplane A Lockheed Martin Missiles and Fire Control-Orlando Business. (date unknown)

Schulz, Timothy J. and Donald L. Snyder. "Image recovery from correlations," *Journal of the Optical Society of America A:* 1266-1270 (August, 1992).

Strum, Robert D. and Donald E. Kirk. *First Principles of Discrete Systems and Digital Signal Processing,* Reading, Massachusetts: Addison-Wesley, 1989

Troph, William J. "Temperature-dependent refractive index models for BaF_2, CaF_2, MgF_2, SrF_2, LiF, NaF, KCl, ZnS, and ZnSe." *Optical Engineering* Vol. 34 No. 5: 1369-1373 (1995)

REPORT DOCUMENTATION PAGE

The public reporting burden for this collection of information is estimated to average 1 hour per response, including the time for reviewing instructions, searching existing data sources, gathering and maintaining the data needed, and completing and reviewing the collection of information. Send comments regarding this burden estimate or any other aspect of the collection of information, including suggestions for reducing this burden to Department of Defense, Washington Headquarters Services, Directorate for Information Operations and Reports (0704-0188), 1215 Jefferson Davis Highway, Suite 1204, Arlington, VA 22202-4302. Respondents should be aware that notwithstanding any other provision of law, no person shall be subject to an penalty for failing to comply with a collection of information if it does not display a currently valid OMB control number.
PLEASE DO NOT RETURN YOUR FORM TO THE ABOVE ADDRESS.

1. REPORT DATE (DD-MM-YYYY) 01-12-2004	2. REPORT TYPE **Master's Thesis**	3. DATES COVERED (From – To) Apr 2004 – Nov 2004

4. TITLE AND SUBTITLE		5a. CONTRACT NUMBER
Design and Model Verification of an Infrared Chromotomographic Imaging System		5b. GRANT NUMBER
		5c. PROGRAM ELEMENT NUMBER
6. AUTHOR(S) LeMaster, Daniel A., Civilian		5d. PROJECT NUMBER
		5e. TASK NUMBER
		5f. WORK UNIT NUMBER

7. PERFORMING ORGANIZATION NAMES(S) AND ADDRESS(S) Air Force Institute of Technology Graduate School of Engineering and Management (AFIT/EN) 2950 Hobson Way WPAFB OH 45433-7765	8. PERFORMING ORGANIZATION REPORT NUMBER AFIT/GAP/ENP/04-06

9. SPONSORING/MONITORING AGENCY NAME(S) AND ADDRESS(ES) N/A	10. SPONSOR/MONITOR'S ACRONYM(S)
	11. SPONSOR/MONITOR'S REPORT NUMBER(S)

12. DISTRIBUTION/AVAILABILITY STATEMENT
APPROVED FOR PUBLIC RELEASE; DISTRIBUTION UNLIMITED.

13. SUPPLEMENTARY NOTES

14. ABSTRACT

A prism chromotomographic hyperspectral imaging sensor is being developed to aid in the study of bomb phenomenology. Reliable chromotomographic reconstruction depends on accurate knowledge of the sensor specific point spread function over all wavelengths of interest. The purpose of this research is to generate the required point spread functions using wave optics techniques and a phase screen model of system aberrations.

The phase screens are generated using the Richardson-Lucy algorithm for extracting point spread functions and Gerchberg-Saxton algorithm for phase retrieval. These phase screens are verified by comparing the modeled results of a blackbody source with measurements made using a chromotomographic sensor. The sensor itself is constructed as part of this research. Comparison between the measured and simulated results is based upon the noise statistics of the measured image.

Four comparisons between measured and modeled data, each made at a different prism rotation angle, provide the basis for the conclusions of this research. Based on these results, the phase screen technique is appears to be valid so long as constraints are placed on the field of view and spectral region over which the screens are applied.

15. SUBJECT TERMS
hyperspectral, prism chromotomography, chromotomographic reconstruction, wave optics, phase screen, infrared, phase reconstruction

16. SECURITY CLASSIFICATION OF:			17. LIMITATION OF ABSTRACT	18. NUMBER OF PAGES	19a. NAME OF RESPONSIBLE PERSON Stephen C. Cain, PhD AFIT/ENG
REPORT U	ABSTRACT U	c. THIS PAGE U	UU	93	19b. TELEPHONE NUMBER (Include area code) (937) 255-6565, ext 4408; e-mail: Stephen.Cain@afit.edu